Importance of anisotropic Coulomb interaction in $LaMnO_3$

Thomas A. Mellan,[1] Furio Corà,[1] Ricardo Grau-Crespo,[2] and Sohrab Ismail-Beigi[3,4]
[1]*Department of Chemistry, University College London, 20 Gordon Street, London WC1H 0AJ, United Kingdom*
[2]*Department of Chemistry, University of Reading, Whiteknights, Reading RG6 6AD, United Kingdom*
[3]*Department of Applied Physics, Yale University, New Haven, Connecticut, USA*
[4]*Center for Research on Interface Structures and Phenomena (CRISP), Yale University, New Haven, Connecticut, USA*
(Received 31 March 2015; revised manuscript received 5 August 2015; published 28 August 2015)

In low-temperature antiferromagnetic $LaMnO_3$, strong and localized electronic interactions among Mn $3d$ electrons prevent a satisfactory description from standard local density and generalized gradient approximations in density functional theory calculations. Here, we show that the strong on-site electronic interactions are described well only by using direct *and* exchange corrections to the intraorbital Coulomb potential. Only DFT + U calculations with explicit exchange corrections produce a balanced picture of electronic, magnetic, and structural observables in agreement with experiment. To understand the reason, a rewriting of the functional form of the $+U$ corrections is presented that leads to a more physical and transparent understanding of the effect of these correction terms. The approach highlights the importance of Hund's coupling (intraorbital exchange) in providing anisotropy across the occupation and energy eigenvalues of the Mn d states. This intraorbital exchange is the key to fully activating the Jahn-Teller distortion, reproducing the experimental band gap and stabilizing the correct magnetic ground state in $LaMnO_3$. The best parameter values for $LaMnO_3$ within the DFT (PBEsol) + U framework are determined to be $U = 8$ eV and $J = 1.9$ eV.

DOI: 10.1103/PhysRevB.92.085151 PACS number(s): 71.15.Mb, 71.20.−b, 75.30.Et, 75.25.Dk

I. INTRODUCTION

$LaMnO_3$ (LMO) is characteristic of the ABO_3 family of strongly correlated transition metal oxide perovskites, which generally exhibit complex phase diagrams, as a result of subtle coupling across several distinct mechanisms [1]: bulk, thin film, and interfacial $LaMnO_3$ are subject to a multitude of symmetry breaking mechanisms, including crystal field [1], octahedral distortion [2], orbital ordering and Jahn-Teller distortion [3–6], Mott-type strong d-electron Coulomb interactions (direct and exchange) [7,8], and charge transfer ordered (Verwey) states [9–11]. All of these mechanisms are believed to exist and compete in varying ways in this material. As a result, $LaMnO_3$ naturally exhibits a rich phase diagram as a function of temperature and pressure [6] as well as dopant concentration [12,13]. These properties make $LaMnO_3$ the single most examined metal oxide in the $LaXO_3$ class (where X is a transition metal atom) [14]. Doping on the ABO_3 A site provides a particularly rich field of experimentally observed phenomena, with both Na and Ca doped $La_{1-x}A_xMnO_3$ exhibiting colossal magnetoresistance (CMR) [15,16] and a Seebeck coefficient that can exhibit positive or negative values, which may lead to potential thermopower applications [17]. Pure bulk $LaMnO_3$ is spin polarized and nonpolar, but recent theoretical work shows that the magnetic state in Sr doped $La_{1-x}Sr_xMnO_3$ may be controlled through variation in the electric polarization state [13]. Recent multiferroic theory predicts novel magnetic properties due to t_{2g} ferromagnetic superexchange in Ti doped LMO interfaces [18]. Finally, the interface between $La_{1-x}Sr_xMnO_3$ and a ferroelectric shows a polar state that also has a reversible orbital polarization [19].

This interest in LMO from condensed matter and materials scientists underscores the value of a reliable first-principles description based on, for example, density functional theory (DFT). In particular, the magnetic, electronic, and crystal structure should be accessible simultaneously within a low-cost computational framework. Unfortunately, previous Hartree-Fock, DFT and hybrid-functional examinations of bulk LMO show that that obtaining a satisfactory description is not trivial [1,20].

In this work, we show the limitations and successes of two different DFT + U methods. The Dudarev *et al.* Coulomb correction [21], here called U_{eff}, averages out exchange effects of the Mn d shell, and we show that it cannot simultaneously reproduce the bulk band gap, structure and magnetism. The dedicated anisotropic exchange term in the Liechtenstein *et al.* Coulomb correction [22], here called $U|J$, dramatically improves the description of LMO. The $U|J$ method answers the specific call for a practical DFT-based methodology capable of reproducing the gap, structure and magnetism simultaneously in LMO [23]. This is useful as understanding the coupling between electronic, magnetic, and lattice degrees of freedom in LMO is a matter of persistent interest [2,23,24].

Using the $U|J$ method, we show the importance of Hund's coupling in LMO. Intraorbital exchange can energetically order the orbitals of the Mn $t_{2g}^3 e_g^1$ ion, which in turn strongly affects *interorbital* magnetism and the size of the LMO band gap. The Mn e_g^1 occupancy polarization [19,25]

$$\pi^{e_g\sigma} = \frac{f_{x^2-y^2\sigma} - f_{3z^2-r^2\sigma}}{f_{x^2-y^2\sigma} + f_{3z^2-r^2\sigma}}, \tag{1}$$

for the $x^2 - y^2$ and $3z^2 - r^2$ occupancy eigenvalues (f) where σ labels spin, is highly sensitive to intraorbital exchange term J in the $U|J$ scheme. By modifying the sign and value of $\pi^{e_g\sigma}$, we correct the DFT description of Jahn-Teller (JT) distortion, and the electronic and magnetic structures of LMO. In addition, the $U|J$ calculations provide insight into the origin of magnetic, electronic, and structural ordering in LMO.

II. METHODOLOGY

Periodic plane-wave density functional theory (DFT) calculations are performed using the VASP software [26,27], the local density approximation (LDA) functional of Perdew and Zunger (PZ81) [28], and the generalized gradient approximation (GGA) in the form of the Perdew-Burke-Erzenhof solids-adapted exchange correlation functional (PBEsol) [29,30]. Valence electrons are described using the projector augmented wave (PAW) method [31,32] with core states (up to $4d$ in La, $2p$ in Mn, and $2s$ in O) frozen at their atomic reference states. Plane waves were cutoff above a kinetic energy of 520 eV, and a $5\times4\times5$ **k**-point mesh was employed for the $LaMnO_3$ unit cells. All relaxed structures fulfill a convergence criterion of less than 0.01 eV/Å, for both ionic forces and volume-normalized stresses (as standard in VASP).

DFT has known shortcomings in the prediction of the electronic structure of materials with localized electronic states [22,33,34]. A typical example are the bands derived from Mn d orbitals in $LaMnO_3$: the errors can be corrected to various extents by employing Hubbard-U type corrections to account for intraatomic Coulomb interactions in the DFT + U approach [21,22,34]. The most popular and simplest Coulomb correction is the "spherically averaged" scheme of Dudarev *et al.* [21], here called DFT + $U_{\rm eff}$, which has only a single effective U parameter, $U_{\rm eff}$. A more sophisticated approach is the "rotationally invariant" scheme of Lichtenstein and Zaanen [22], which we label here as DFT + $U|J$. Note the simpler Dudarev $U_{\rm eff}$ approach was developed after the Liechtenstein $U|J$ approach, and both are fully rotationally invariant.

Both DFT + U methodologies add Hartree-Fock type corrections to the DFT total energy that act on a local subspace of atomiclike orbitals. The DFT + $U_{\rm eff}$ total energy is given by

$$E_{\mathrm{DFT}+U_{\mathrm{eff}}} = E_{\mathrm{DFT}} + \frac{U_{\mathrm{eff}}}{2}\sum_{at}\sum_{i,\sigma}\left(f_{i\sigma} - f_{i\sigma}^2\right), \qquad (2)$$

where $E_{\rm DFT}$ refers to some chosen flavor of electron density-based exchange-correlation approximation (LDA or GGA in our work). The index at specifies the Mn sites where the correction is performed. The eigenoccupations $f_{i\sigma}$ of the electronic on-site density matrix are labeled by spin σ and index i which represents a linear combination of angular momentum quantum numbers (which in our case ranges over the five magnetic quantum numbers $m = -2, -1, 0, 1, 2$ for the $3d$ Mn orbitals). $U_{\rm eff} = U - J$ is the Hubbard-type energy parameter for this approach while U and J are the separate direct and exchange Coulomb parameters [22] (see also Appendix A).

For our work here, the DFT + $U|J$ total energy is best rewritten as an added correction to the DFT + $U_{\rm eff}$ approach (as detailed in Appendix A) given by

$$\begin{aligned} E_{\mathrm{DFT}+U|J} &= E_{\mathrm{DFT}} + E_{\mathrm{corr}} \\ &= E_{\mathrm{DFT}} + \frac{U_{\mathrm{eff}}}{2}\sum_{at}\sum_{i,\sigma}\left(f_{i\sigma} - f_{i\sigma}^2\right) \\ &\quad + \frac{1}{2}\sum_{\sigma\sigma',ij} \mathrm{C}_{ij}^{\sigma\sigma'} f_{i\sigma} f_{j\sigma'} - \Delta\mathrm{X}_{ij}^{\sigma} f_{i\sigma} f_{j\sigma}\delta_{\sigma\sigma'}. \end{aligned} \qquad (3)$$

The correction to the DFT band energy eigenvalue $\epsilon_{i\sigma}$ stems from the occupancy derivative of the correction terms given by

$$\begin{aligned} \Delta\epsilon_{i\sigma}^{\mathrm{corr}} &= \frac{\partial E_{\mathrm{corr}}}{\partial f_{i\sigma}} = U_{\mathrm{eff}}\left(\frac{1}{2} - f_{i\sigma}\right) \\ &\quad + \sum_{j,\sigma'} \mathrm{C}_{ij}^{\sigma\sigma'} f_{j\sigma'} - \Delta\mathrm{X}_{ij}^{\sigma} f_{j\sigma}\delta_{\sigma\sigma'}, \end{aligned}$$

where the first term is the $U_{\rm eff}$ correction and the second and third terms are the added contribution from the $U|J$ scheme. For compactness and for use below, it is useful to collect all occupancies or energy eigenvalues for the same spin into a vector f_σ or ϵ_σ in order to write these corrections in matrix notation. For atomic d shells, the Appendix A shows that

$$\Delta\epsilon_{\sigma}^{\mathrm{corr}} = U_{\mathrm{eff}}\left(\tfrac{1}{2} - f_\sigma\right) + J\mathrm{A}^{\sigma} f_\sigma + J\mathrm{B}^{\sigma} f_{\bar\sigma}, \qquad (4)$$

where $\bar\sigma$ represents the opposite spin to σ. For canonical t_{2g} and e_g orbitals, the dimensionless matrices A^σ and B^σ are

$$\mathrm{A}^{\sigma} = \begin{array}{c|ccccc} & 3z^2-r^2 & x^2-y^2 & xy & yz & xz \\ \hline 3z^2-r^2 & 0 & -0.52 & -0.52 & 0.52 & 0.52 \\ x^2-y^2 & -0.52 & 0 & 0.86 & -0.17 & -0.17 \\ xy & -0.52 & 0.86 & 0 & -0.17 & -0.17 \\ yz & 0.52 & -0.17 & -0.17 & 0 & -0.17 \\ xz & 0.52 & -0.17 & -0.17 & -0.17 & 0 \end{array}$$

and

$$\mathrm{B}^{\sigma} = \begin{array}{c|ccccc} & 3z^2-r^2 & x^2-y^2 & xy & yz & xz \\ \hline 3z^2-r^2 & 1.14 & -0.63 & -0.63 & 0.06 & 0.06 \\ x^2-y^2 & -0.63 & 1.14 & 0.29 & -0.40 & -0.40 \\ xy & -0.63 & 0.29 & 1.14 & -0.40 & -0.40 \\ yz & 0.06 & -0.40 & -0.40 & 1.14 & -0.40 \\ xz & 0.06 & -0.40 & -0.40 & -0.40 & 1.14 \end{array}.$$

Both DFT + U methodologies permit the description of electron localization phenomena, that stem from Hartree-Fock physics and the related removal of self-interaction errors, which enable essential long-range ordering (orbital, spin,

charge and lattice degrees of freedom) [33]. For Mn in LMO, delocalized s and p orbitals typify the weakly correlated electronic states successfully described by DFT, while the localized Mn d states require the $+U$ correction. In the DFT $+ U_{\text{eff}}$ approach, U_{eff} in Eq. (2) provides occupation-dependent corrections to DFT, while the DFT $+ U|J$ approach in Eq. (3) adds further degrees of explicit spatial/orbital dependent corrections. Both corrections provide a basis for for energy splitting of d orbitals (and related symmetry breaking and orbital polarization) on top of splittings due to spin exchange and/or crystalline geometrical distortions already present at the LDA or GGA density functional level.

The $U|J$ correction variety in Eq. (4) is most relevant to materials with strongly interacting electrons with an explicit orbital symmetry dependence [35], for example, Fe-based superconductors [36], heavy fermion metals [37], noncollinear magnetic materials [38,39], and orbitally ordered materials in which Hund's coupling is critical to establishing the correct insulating or metallic character [40]. Although the anisotropic exchange corrections to DFT have successfully been used to describe manganese oxides in the past [39,41,42], we believe our work is the first explicit calculation and analysis of the $U|J$ exchange matrix elements and anisotropic splitting for $LaMnO_3$.

In our work, our global coordinate system is chosen to align the orthogonal $x',y,'z'$ axes along the LMO unit cell (a,b,c) vectors. A local x,y,z basis for each Mn is defined by aligning the local axes with the Mn-O bonds of each tilted MnO_6 octahedron (see Figs. 1 and 4): the local x axis is chosen along the shortest Mn-O bond (strongly JT active), the local y axis along the intermediate length Mn-O bond (here called apical), and the local z axis is along the longest Mn-O bond (strongly JT active). Use of this local basis is more convenient for analysis of the electronic states and occupancies. The transformation from global to local coordinates is performed for each relaxed geometry by employing a direct polynomial-based transformation of orbitals (detailed in Appendix B). Unless specifically noted, orbitals and occupancies refer to the local basis.

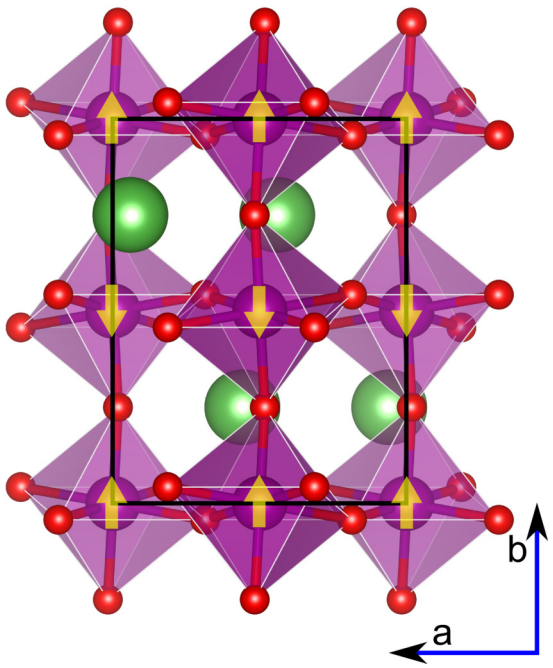

FIG. 1. (Color online) (001) face of A-type antiferromagnetic (A-AFM) $LaMnO_3$: Mn in purple, La in green, and O in red. Arrows indicate direction of spin polarization on Mn ions.

III. RESULTS AND DISCUSSION

At 750 K, $LaMnO_3$ (LMO) undergoes a structural phase transition, transforming from cubic to orthorhombic symmetry. Under ambient conditions the orthorhombic perovskite has a paramagnetic spin structure. Below the Néel temperature of $T_N \approx 140$ K [43], LMO is an insulator with A-type antiferromagnetic (A-AFM) spin ordering. For the low-temperature orthorhombic ($Pnma$) LMO structure shown in Fig. 1, experimental reports of lattice parameters are $a = 5.736$ Å, $b = 7.703$ Å, and $c = 5.540$ Å by neutron powder diffraction [44]. To support the A-AFM ordering in $LaMnO_3$, the Mn d^4 electrons exchange anisotropically: ferromagnetic (FM) coupling exists between Mn in {010} planes while AFM coupling exists between successive planes along [010].

The reported experimental band gaps in LMO cover a range of values, depending on whether the gap is determined from measurements on conductivity (0.24 eV) [17], optical absorption (1.1 eV) [45], photoemission (1.7 eV) [46], optical conductivity (1.9 eV) [47], or resonant Raman spectroscopy (2 eV) [48]. DFT is a single-particle theory, so even with the exact exchange-correlation functional, it can only describe the fundamental (quasiparticle) band gap and not the optical one. We therefore consider the most appropriate reference value to be the 1.7-eV photoemission gap measured by Saitoh *et al.* [46]. We note that recent computational work by Lee *et al.* [49] predicts a direct gap of 1.1 eV, in agreement with the optical absorption gap of 1.1 eV measured by Arima *et al.* [45]. The value of the optical gap is generally lower than the fundamental gap due to electron-hole interactions (i.e., excitonic effects). Such two-particle interactions are not included in standard one-particle DFT, so we believe the most reliable comparisons should be made between a benchmark indirect experimental photoemission gap such as the 1.7-eV Saitoh gap [46] and the indirect DFT gap.

One of our main practical considerations here is to reproduce the different facets of the above experimental description. To do this, DFT calculations are performed screening through different levels of Coulombic localisation.

A. Description of $LaMnO_3$ using DFT $+ U$

Previous work has applied the single term U_{eff} approach to calculations on bulk $LaMnO_3$ [1,13,23,50]. The failure of this approach to *simultaneously* describe the energy gap, structure and magnetism drives us to systematically examine the U_{eff} method. These initial results also provide context for the more sophisticated $U|J$ method and analysis of its merits and behavior below.

1. *Experimental* $LaMnO_3$ *structure via* DFT $+ U_{\text{eff}}$

Standard LDA (PZ81) and GGA (PBEsol) with $U_{\text{eff}} = 0$ eV both successfully stabilize the low-temperature experimental A-AFM ordering as shown in Table I. However, this is

TABLE I. LDA + U_{eff} and GGA + U_{eff} results for the energy gap E^{Gap} (in eV), for the A-AFM and FM phases, and the total energy difference $\Delta E = E^{\text{A-AFM}} - E^{\text{FM}}$ (in meV) per formula unit of $LaMnO_3$. The crystal structure is held fixed at the experimental geometry.

	LDA (PZ81)			GGA (PBEsol)		
U_{eff} (eV)	$E^{\text{Gap}}_{\text{A-AFM}}$	$\Delta^{\text{Gap}}_{\text{FM}}$	ΔE	$E^{\text{Gap}}_{\text{A-AFM}}$	$\Delta^{\text{Gap}}_{\text{FM}}$	ΔE
0	0.0	0.0	− 22	0.2	0.0	− 13
2	0.5	0.0	− 5	0.6	0.0	1
4	1.0	0.0	4	1.0	0.0	8
6	1.3	0.1	10	1.3	0.1	14
8	1.4	0.2	14	1.4	0.2	17

essentially where the success ends. As noted previously, both GGA and LDA are unable to produce significant orbital splitting (beyond some aspects due to spin exchange and structural distortion) and also exaggerate electron delocalization due to inexact exchange (or equivalently lack of self-interaction correction). This inevitably results in a qualitatively incorrect electronic structure with a seriously underestimated band gap: both GGA and LDA with $U_{\text{eff}} = 0$ eV yield band gaps that are far too small compared to experiment.

Increasing U_{eff} stabilizes the occupied ($f_{i\sigma} \gtrsim \frac{1}{2}$) eigenstates and drives orbital occupations toward binary polarization: filled states become more filled and empty states more empty. For example, increasing U_{eff} from 0 to 8 eV in GGA calculations results in the following change in occupancies in the Mn d manifold:

$$(f_\sigma \,|\, f_{\bar{\sigma}}) = \left(\begin{array}{c|c} 0.65 & 0.22 \\ 0.73 & 0.26 \\ 0.93 & 0.11 \\ 0.93 & 0.10 \\ 0.93 & 0.09 \end{array}\right) \rightarrow \left(\begin{array}{c|c} 1.00 & 0.10 \\ 0.57 & 0.17 \\ 0.98 & 0.04 \\ 0.97 & 0.03 \\ 0.97 & 0.04 \end{array}\right), \qquad (5)$$

where the ordering of orbitals in the local basis is $\begin{pmatrix} 3z^2 - r^2 \\ x^2 - y^2 \\ xy \\ yz \\ xz \end{pmatrix}$.

The Hubbard limit of very large U_{eff} typically favours FM coupling in $LaMnO_3$ [4], and Table I confirms this. The primary reason is that increasing U_{eff} kills the superexchange mechanism, which scales as $\sim t^2/U_{\text{eff}}$, where t is the effective Mn-Mn hopping, and this mechanism underlies the stability of A-AFM ordering in $LaMnO_3$. As a result, e_g double-exchange is relatively strengthened and we find FM ordering. Critically, Table I shows that a large U_{eff} value is required to open a satisfactory energy gap. Unfortunately, this situation results in a trade-off between correct gap or correct magnetism.

2. *Relaxed* $LaMnO_3$ *structure via* DFT + U_{eff}

When we permit the structure of $LaMnO_3$ to fully relax during the calculation, we obtain the results in Table II. Having a nonzero U_{eff} improves the crystal geometry and the electronic structure description for both GGA and LDA. Particular improvements are for the large erroneous distortion in a (insufficient orthorhombic character) and the opening of the band gap. Figure 2 and Table II show that the band gap increases roughly linearly with U_{eff} at first but then tails off at higher U_{eff}. The ineffectiveness of U_{eff} at high values is shown in Fig. 2, and can be understood in terms of the partial $x^2 - y^2$ occupation shown in Eq. (5). The partial $x^2 - y^2$ occupation damps the impact of U_{eff} on the energy eigenvalue splittings since $\Delta\epsilon_{x^2-y^2\sigma} = U_{\text{eff}}(\frac{1}{2} - f_{x^2-y^2\sigma}) \approx 0$ for $f_{x^2-y^2\sigma} \approx \frac{1}{2}$. (The reason partial e_g occupation occurs is that the d manifold is not isolated but connected to the rest of the system *via* hybridization to the O $2p$ orbitals, or in other words due to the partial covalency of the Mn-O bond.)

Although adding U_{eff} to GGA and LDA produces similar band gaps as per Table II, the GGA + U_{eff} geometry is preferable. Overall, a high value of $U_{\text{eff}} \sim$ 6 eV, correcting the GGA formalism, provides on balance the best gap/structure combination. Again, an evident failure of U_{eff} is its inability to predict the correct magnetic ordering at the U_{eff} level required to correct the structure and the band gap.

3. *Experimental* $LaMnO_3$ *structure via* DFT + $U|J$

Following the failure of the U_{eff} scheme in both single-point and relaxed geometry calculations, we turn to the DFT + $U|J$ methodology. The U_{eff} results conveniently suggest a reasonable starting point: since $U_{\text{eff}} = U - J$, an $U|J$ correction with magnitude of approximately $U - J \approx 6$ eV is appropriate. Results in Table III are for bulk $LaMnO_3$ at the experimental structure, and sampling J from 0 to 3 eV in conjunction with U from 6 to 8 eV. Increasing J for a fixed value of U stabilizes A-AFM ordering and enhances orbital splitting which further opens the band gap. Orbital splittings due to the U_{eff} are generally "isotropic" in that they are based solely on the occupation. The marked improvement by the $U|J$ method emphasizes the importance of explicit spatial exchange

TABLE II. Band gap E^{Gap}, total energy difference $\Delta E = E^{\text{A-AFM}} - E^{\text{FM}}$ per unit cell, and percent errors, with respect to experiment, for lattice parameters and unit cell volume of fully relaxed A-AFM bulk $LaMnO_3$.

	LDA (PZ81)						GGA (PBEsol)					
U_{eff} (eV)	E^{Gap} (eV)	Δ^{a} (%)	Δ^{b} (%)	Δ^{c} (%)	$\Delta^{\text{Vol.}}$ (%)	ΔE(meV)	E^{Gap} (eV)	Δ^{a} (%)	Δ^{b} (%)	Δ^{c} (%)	$\Delta^{\text{Vol.}}$ (%)	ΔE(meV)
0	0.00	− 5.8	− 3.0	− 1.2	− 9.8	54	0.00	− 3.5	− 0.6	− 0.3	− 4.4	34
2	0.22	− 2.9	− 1.6	− 1.1	− 5.5	52	0.48	− 0.6	− 0.8	− 0.5	− 1.9	47
4	0.81	− 1.8	− 1.6	− 1.1	− 4.4	25	0.92	− 0.0	− 0.5	− 0.3	− 0.9	19
6	1.13	− 1.5	− 1.0	− 1.0	− 3.5	13	1.10	0.2	− 0.1	− 0.3	− 0.1	19
8	1.23	− 1.4	− 0.6	− 1.0	− 3.0	19	1.08	0.4	0.4	− 0.2	0.6	27

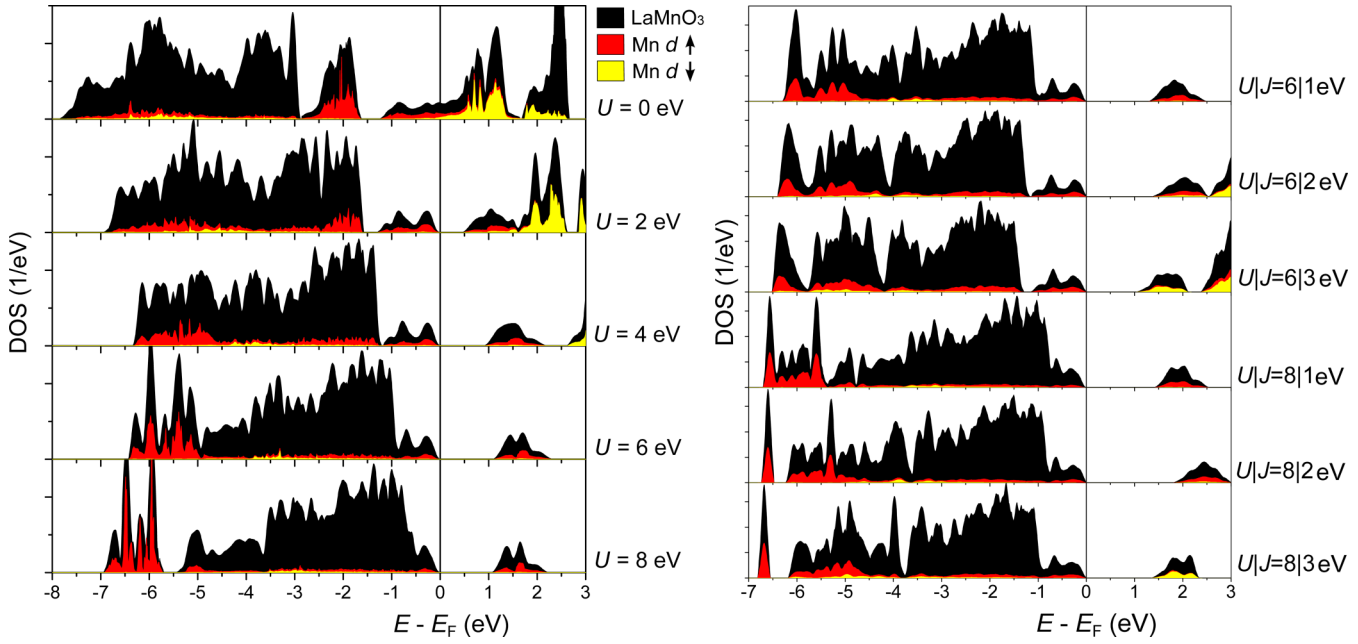

FIG. 2. (Color online) U_{eff} (left) and $U|J$(right) corrected density of states for fully relaxed A-AFM $LaMnO_3$ as a function of energy, $E - E_F$. Black curves show the total density of states while red and yellow curves show Mn d majority spin and minority spin densities of states.

anisotropy in the $LaMnO_3$ Mn d manifold. The results in Table III are encouraging, but since distortion of the lattice is critical in $LaMnO_3$ [2], the trends observed must be verified by fully relaxing ionic positions and lattice parameters, which we report on next.

4. *Relaxed* $LaMnO_3$ *structure via* DFT + $U|J$

Table IV displays key data for fully relaxed bulk $LaMnO_3$ using the DFT + $U|J$ framework. Relaxed results largely echo the experimental structure results above for A-AFM $LaMnO_3$, with the $U|J$ combination of $U = 8$ eV and $J = 2$ eV providing a good overall description. In particular the $U|J = 8|2$ eV combination provides agreement in terms of electronic, magnetic and structural observables from experiment [44,46,47,51] and also more computationally expensive many-body GW approximation [52] results. Volume errors $<1\%$ improve on previous work [23,44,51], and the error in energy gap is small at approximately $\sim 5\,\%$ (<0.1 eV error) [46]. In addition, the A-AFM ordering is stabilized against FM ordering, which was previously seen as a missing ingredient [23,24]. The improvements in LMO description depend intimately on the intraorbital exchange description—this is explored further by quantifying the action of the Hund's coupling interaction on the LMO Mn d states.

TABLE III. Results from GGA (PBEsol) + $U|J$ for the experimental geometry of bulk $LaMnO_3$. Band gaps E^{Gap} are in eV for each magnetic state, and $\Delta E = E^{\text{A-AFM}} - E^{\text{FM}}$ is the total energy difference per unit cell between the two magnetic phases.

$U\|J$ (eV)	$E^{\text{Gap}}_{\text{A-AFM}}$ (eV)	$E^{\text{Gap}}_{\text{FM}}$ (eV)	ΔE(meV)
6|0	1.3	0.1	14
6|1	1.3	0.2	6
6|2	1.2	0.4	− 10
6|3	0.6	0.2	− 39
8|0	1.4	0.2	17
8|1	1.5	0.4	11
8|2	1.6	0.8	− 2
8|3	1.0	0.5	− 32

TABLE IV. Fully relaxed $LaMnO_3$ results based on GGA (PBEsol) + $U|J$. Band gaps E^{Gap}, lattice parameter errors, and total energy differences between the A-AFM and FM magnetic phases $\Delta E = E^{\text{A-AFM}} - E^{\text{FM}}$ per formula unit are listed.

	A-AFM					
$U\|J$ (eV)	E^{Gap} (eV)	Δ^{a} (%)	Δ^{b} (%)	Δ^{c} (%)	$\Delta^{\text{Vol.}}$ (%)	ΔE (meV)
6|0	1.1	0.4	− 0.1	− 0.4	0.0	19
6|0.5	1.2	0.6	− 0.4	− 0.4	− 0.2	14
6|1	1.3	0.9	− 0.7	− 0.5	− 0.3	7
6|1.5	1.4	1.2	− 0.9	− 0.6	− 0.3	− 1
6|2	1.4	0.8	− 1.2	0.1	− 0.4	− 10
6|2.5	1.3	1.8	− 1.3	− 0.8	− 0.2	− 21
7|0	1.2	0.5	0.1	− 0.3	0.3	23
7|0.5	1.3	0.7	− 0.2	− 0.4	0.2	17
7|1	1.4	0.9	− 0.5	− 0.5	0.0	11
7|1.5	1.5	1.2	− 0.7	− 0.5	− 0.1	3
7|2	1.6	1.6	− 1.0	− 0.7	0.0	− 6
7|2.5	1.5	1.9	− 1.2	− 0.7	− 0.1	− 17
8|0	1.1	0.5	0.4	− 0.3	0.6	27
8|0.5	1.2	0.6	0.1	− 0.3	0.4	21
8|1	1.4	1.0	− 0.2	− 0.5	0.3	15
8|1.5	1.6	1.2	− 0.5	− 0.5	0.1	7
8|2	1.8	1.5	− 0.8	− 0.6	0.1	− 2
8|2.5	1.7	1.7	− 1.0	− 0.6	0.1	− 14

B. Explicit exchange anisotropy in Mn3+

Strong on-site Coulomb repulsion is the central theme in paradigms of "Mottness" and electron localization. However, the importance of Hund's coupling (intraorbital exchange) in materials with partial d-and f-shell occupations has been highlighted [53]. In this section, we attempt to understand the nature of Hund's coupling in LMO, by examining the effects of the on-site exchange terms as defined in Appendix A. We explore why the $U|J$ methodology can describe $LaMnO_3$ adequately, reproducing band gap and correct magnetic ground state simultaneously. We employ a simple model where we focus only on the occupancies of the Mn^{3+} d^4 manifold in order to isolate the effect of the exchange J parameter (and related physics) on the Mn d states as per Eq. (4). Majority-spin t_{2g}^3 states are generally fully occupied due to the strong exchange splitting between spin channels, and as is well known, increasing U increases occupancy polarization. However, the nature of anisotropic interactions in the Mn d-shell due to J is less well understood, particularly with respect to the polarization of the e_g^1 occupation into $3z^2-r^2$ or x^2-y^2 (or some mix of the two).

We begin with three model e_g^1 occupations, $\pi^{e_g}=0,\pm1$, in an attempt to pinpoint what J really does and understand the nature of Hund's coupling in different limits. As a reminder, π^{e_g} is the e_g occupancy polarization as defined in Eq. (1). After examining these model systems, we will consider the effect of J in the actual calculations where we use the calculated *ab initio* occupations together with our analytical rewriting of the $U|J$ energy function and eigenvalue corrections. As explained above, the e_g and t_{2g} group terms discussed correspond to the local octahedral basis (i.e., post rotation as per Appendix B).

1. Anisotropic exchange for model orbital occupations

To illustrate the anisotropic effects of the J terms in the $U|J$ schema, we begin with a set of model occupancies where we fix the formal occupation of Mn^{3+} (d^4) but vary the orbital polarization. A $\pi^{e_g}=+1$ model polarization corresponds to a single hole on the majority spin $3z^2-r^2$ site (i.e., $f_{x^2-y^2\sigma}=f_{t_{2g}\sigma}=1$, $f_{3z^2-r^2\sigma}=0$, and $f_{\bar{\sigma}}=0$). Based on Eq. (4), the added effect of the exchange J terms is to create additional energy splittings (beyond simple occupancy polarization proportional to U_{eff}) given by

$$\pi^{e_g}=+1:(\Delta\epsilon_\sigma|\Delta\epsilon_{\bar{\sigma}})=J\cdot\left(\begin{array}{c|c}0.00&-1.14\\0.52&0.63\\0.52&0.63\\-0.52&-0.06\\-0.52&-0.06\end{array}\right). \quad (6)$$

The opposite polarity, $\pi^{e_g}=-1$, corresponds to a single hole on the majority spin x^2-y^2 site (that is, $f_{3z^2-r^2\sigma}=f_{t_{2g}\sigma}=1$, $f_{x^2-y^2\sigma}=0$, and $f_{\bar{\sigma}}=0$). This results in the following exchange energy splittings:

$$\pi^{e_g}=-1:(\Delta\epsilon_\sigma|\Delta\epsilon_{\bar{\sigma}})=J\cdot\left(\begin{array}{c|c}0.52&0.63\\0.00&-1.14\\-0.86&-0.29\\0.17&0.40\\0.17&0.40\end{array}\right). \quad (7)$$

Removing the polarization, $\pi^{e_g}=0$, the single hole is equally spread over the two majority spin e_g sites ($f_{e_g\sigma}=0.5$, $f_{t_{2g}\sigma}=1$, and $f_{\bar{\sigma}}=0$). This leads to the splittings

$$\pi^{e_g}=0:(\Delta\epsilon_\sigma|\Delta\epsilon_{\bar{\sigma}})=J\cdot\left(\begin{array}{c|c}0.26&-0.26\\0.26&-0.26\\-0.17&0.17\\-0.17&0.17\\-0.17&0.17\end{array}\right). \quad (8)$$

To visualize these results, we display a schematic showing these splittings in these three cases of $\pi^{e_g}=0,\pm1$ in Fig. 3 where the corrections due to both U and J are shown.

These model results together with the Fig. 3 clearly point out that the effect of the J terms is explicitly anisotropic and its anisotropy and precise value depends on the orbital polarization (which may have been present due the action of the U_{eff} term). The anisotropy exists across both the magnetic

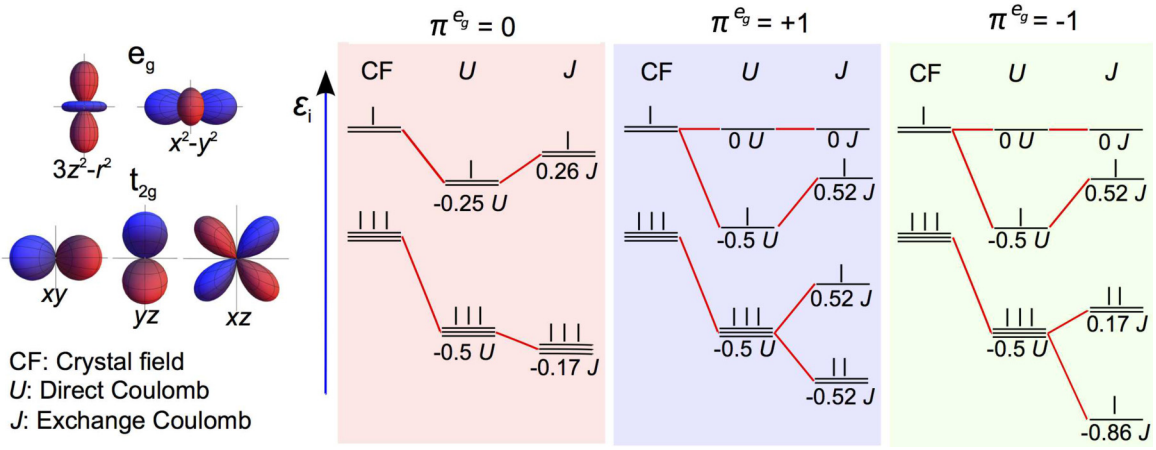

FIG. 3. (Color online) The occupation of states is represented in the model Mn^{3+} d^4 manifold (majority spin only). Orbital degeneracy is broken by octahedral crystal field (CF), Coulomb repulsion U_{eff} (U in the figure) and exchange J following Eq. (4). Each vertical bar represents one unit of electron occupation. $\pi^{e_g\sigma}$ (denoted π^{e_g} for the majority spin channel in the figure) is defined in Eq. (1), and three limits are examined: $\pi^{e_g\sigma}=0$ ($f_{x^2-y^2\sigma}=f_{3z^2-r^2\sigma}=0.5$), $\pi^{e_g\sigma}=+1$ ($f_{x^2-y^2\sigma}=f_{3z^2-r^2\sigma}+1=1$), and $\pi^{e_g\sigma}=-1$ ($f_{x^2-y^2\sigma}+1=f_{3z^2-r^2\sigma}=1$).

quantum number and spin channels (σ and $\bar{\sigma}$). We now discuss these three cases in more detail.

When we have full e_g orbital polarization, i.e., $\pi^{e_g} = \pm 1$, each polarity produces a unique splitting pattern where the magnitude of anisotropy depends on the sign of π^{e_g}. This is despite the fact that $3z^2 - r^2$ and $x^2 - y^2$ states both have e_g symmetry: as we can see that occupying each one (separately) splits the t_{2g} quite differently. This difference is due to fact that the $x^2 - y^2$ state is symmetry related to the t_{2g} states (it is the xy state rotated by $\pi/4$ about the z axis). For example, when $x^2 - y^2$ is fully occupied, the splittings for $x^2 - y^2$ and xy are identical but differ from the other orbitals, but the same is not true when $3z^2 - r^2$ is filled instead. Interestingly, $\sum_{i\sigma} \Delta\epsilon_{i\sigma} f_{i\sigma} = 0$ when $\pi^{e_g} = \pm 1$: this indicates that neither polarization is energetically preferred by intraorbital J terms.

With zero e_g orbital polarization, i.e., $\pi^{e_g} = 0$, we find that this degeneracy inhibits anisotropy from the J terms: the splitting *within* each t_{2g} and e_g manifold is isotropic for both spin channels. The action of the J terms in this situation is to shift the energies of this manifold *en masse*. Here, $\sum_{i\sigma} \Delta\epsilon_{i\sigma} f_{i\sigma} = -0.26J$ when $\pi^{e_g} = 0$ compared to zero for $\pi^{e_g} = \pm 1$.Hence the anisotropic exchange terms in isolation actually favor degenerate occupancy. This result appears to be counterintuitive given the importance of J to anisotropy. The resolution is that we have a much larger and dominant direct Coulomb term U that produces orbital polarization in the first place; the weaker J terms then further enlarge the polarization and make the system more anisotropic. Table V shows this behavior numerically.

In brief, we see that J acting alone energetically *favors degeneracy*. However, with a strong U term already creating orbital polarization, the J terms provide the enlarged anisotropic splitting that one finds in the final results of the calculation.

2. *Anisotropic exchange for ab initio orbital occupations*

For the *ab initio* orbital occupations, we use the DFT + $U|J = 8|2$ eV calculation results, which yield an occupation-polarized e_g manifold as shown in Table V. The e_g polarity is found to be orbitally ordered across the $LaMnO_3$ unit cell as shown in Fig. 4. We now examine this situation in more detail.

TABLE V. Orbital occupation polarization, $\pi^{e_g\sigma}$, for fully relaxed $LaMnO_3$ within the U_{eff} and $U|J$ approaches. Majority spin are σ and minority spin are $\bar{\sigma}$.

Correction (eV)	Same-spin polarization, $\pi^{e_g\sigma}$	Opposite-spin polarization, $\pi^{e_g\bar{\sigma}}$
$U_{\text{eff}} = 0$	0.06	0.08
$U_{\text{eff}} = 8$	−0.27	0.25
$U\|J = 8\|1$	−0.33	0.41
$U\|J = 8\|2$	−0.41	0.54
$U\|J = 8\|3$	−0.52	0.65

The Mn d occupancies from the $U|J = 8|2$ eV method with relaxed geometry are

$$(f_\sigma | f_{\bar{\sigma}}) = \left(\begin{array}{c|c} 0.99 & 0.10 \\ 0.41 & 0.33 \\ 0.98 & 0.06 \\ 0.96 & 0.04 \\ 0.97 & 0.05 \end{array}\right). \tag{9}$$

These occupancies correspond to $\pi^{e_g\sigma} = -0.41$ (from $f_{3z^2-r^2\sigma} = 0.99$ and $f_{x^2-y^2\sigma} = 0.41$). The Mn d shell obviously has more electrons than the model system above, which was based on formal occupancies for Mn^{3+}. Again, we note that this increase is due to hybridization of the Mn d orbitals with the neighboring O $2p$ orbitals, which admixes some Mn d into the low-energy occupied valence states and increases the electron count. Put differently, the itineracy due to the kinetic energy minimization competes with the "Hubbard-esque" Coulomb repulsion and we reach a balance. Numerically, for $U|J = 8|2$ eV, the oxidation state based on the above Mn d occupations can be calculated to be 2.12+ (an alternative or complementary Bader charge picture yields an oxidation state of 1.68+, still less than the formal 3+).

The $U|J = 8|2$ eV occupancies of Eq. (9) result in energy splitting beyond the splitting from U_{eff} alone:

$$(\Delta\epsilon_\sigma | \Delta\epsilon_{\bar{\sigma}}) = J \cdot \left(\begin{array}{c|c} 0.15 & 0.20 \\ 0.30 & -0.65 \\ -0.41 & -0.06 \\ -0.03 & 0.18 \\ -0.01 & 0.20 \end{array}\right). \tag{10}$$

The e_g occupancy polarization of the $U|J = 8|2$ eV calculation is considerably weaker than the previous model cases. Nevertheless, it is large enough to drive significant anisotropic exchange splittings in Eq. (10). For example, the splittings are anisotropic within the majority spin t_{2g} manifold: the xy state is pushed down by approximately $0.4J$ compared to the other two t_{2g} states. Within the e_g manifold, the fully occupied $3z^2 - r^2$ state is pushed up by $0.15J$ while the partially occupied $x^2 - y^2$ state is pushed up considerably more by $0.30J$.

The direct Coulomb interaction U obviously increases π^{e_g}, as expected from the standard instability condition for orbital polarization [23,54],

$$U_{\text{eff}} \times D^\sigma(E_{\text{F}}) \gg 1\,,$$

where $D^\sigma(E_{\text{F}})$ is the density of states in the σ spin channel at the Fermi level. The origin of the monotonic relation between π^{e_g} and J, shown in Table V, is less obvious as J is naïvely expected to drive the electronic structure away from orbital polarization as $U_{\text{eff}} = U - J$. However, π^{e_g} does increase with J, for the above-noted reason that J alone may favor orbital degeneracy but J is strongly anisotropic when in conjunction with a large U value, resulting in the unequal upward "push" of the two e_g orbitals with increasing J. That J and π^{e_g} are so strongly coupled in this material is interesting, as the band gap, Jahn-Teller distortions, and intersite magnetic couplings all depend on π^{e_g}.

As first examined by Kugel and Khomskiĭ [55], e_g^1 occupation polarization (i.e., an electron-electron Jahn-Teller

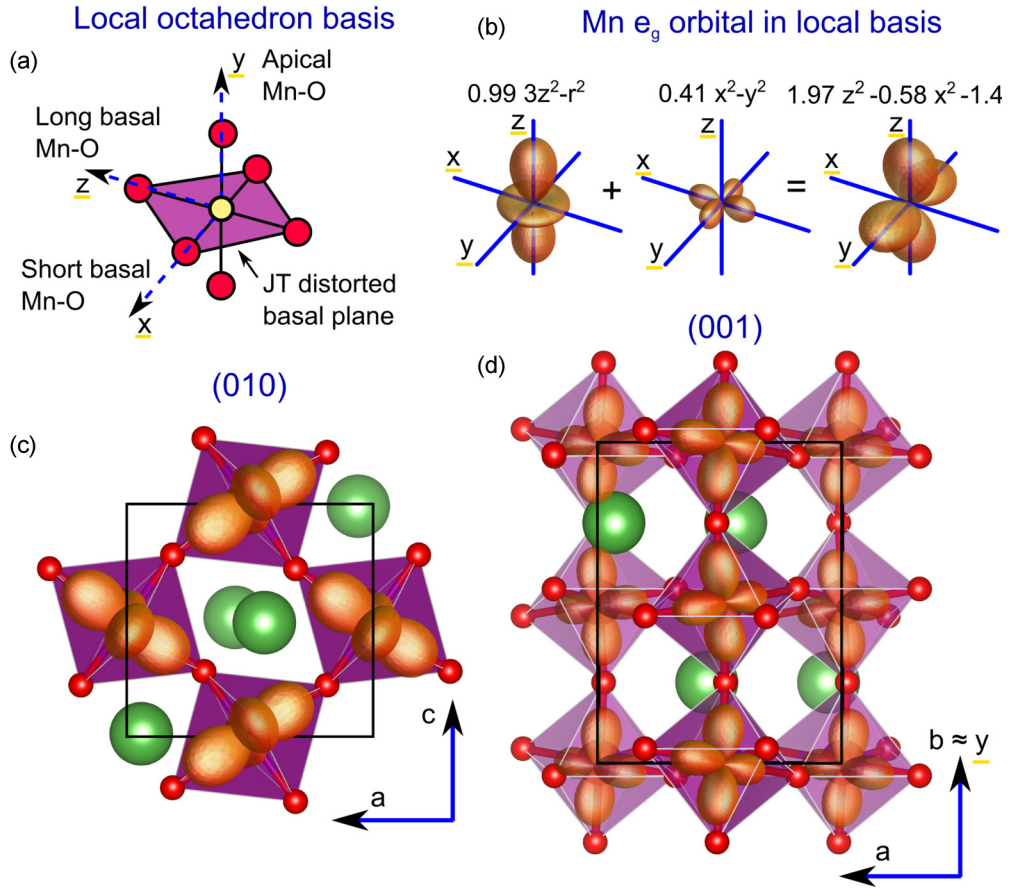

FIG. 4. (Color online) Orbitals in the $LaMnO_3$ unit cell from a $U|J = 8|2$ eV calculation. (a) MnO_6 octahedron with Jahn-Teller distorted plane and local basis vectors labeled. (b) Visualization of the occupation of the $3z^2 - r^2$ and $x^2 - y^2$ states in the rotated basis of the density matrix as well as their superposition for the total local e_g occupancy (plotting the occupation times the orbital expressed in spherical harmonics). (c) The ordering of the occupied e_g shell ($1.97z^2 - 0.58x^2 - 1.4y^2$) in the (010) Jahn-Teller distorted FM coupled plane. (d) The ordering of the occupied e_g shell in the (001) plane with AFM coupling along b. Note x,y,z is the local octahedron basis, and a,b,c lattice vectors correspond to x',y',z' global (prerotation) calculation basis.

degeneracy breaking) enhances virtual superexchange interactions, relative to kinetic exchange interactions such as FM double exchange. This competition between superexchange and double-exchange is observed in the LMO magnetic ground state, which varies according to the magnitude of π^{e_g} (e_g occupancy polarization). π^{e_g} increases with J, which explains the flip in long-range magnetic ordering of the ground state from FM to A-AFM as the intraorbital parameter J is increased.

At $J = 2$ eV, the value of π^{e_g} in Table V is large enough to stabilize the correct A-AFM ordering (as per Table IV). The $U|J = 8|2$ A-AFM ground state in Fig. 1 corresponds to a $0.99(3z^2 - r^2) + 0.41(x^2 - y^2)$ e_g occupation density in the local octahedral basis. The orbital ordering pattern across the unit cell is shown in Fig. 4, and can be rationalized in terms of the Goodenough-Kanamori superexchange rules [56,57].

The $0.99(3z^2 - r^2) + 0.41(x^2 - y^2)$ e_g occupation density can be rewritten as $1.97z^2 - 0.58x^2 - 1.4y^2$. This expression shows the anisotropy in the e_g state, in particular, between the z and x directions in the octahedron: the z^2 contribution is much larger than x^2, as per Fig. 4(b). Each octahedral frame in the ac plane is related to its neighbor by a $\pi/2$ rotation about the b lattice vector, so z^2/x^2 anisotropy forms a checkerboard pattern of e_g partial occupation in the ac plane. Note that this corresponds to the long/short Jahn-Teller Mn-O pattern in the ac plane, as per Fig. 4(c). According to the Goodenough-Kanamori rules, superexchange in the ac plane is determined by z^2/x^2 anisotropy in the e_g partial occupation, and results in the FM coupling in the ac plane.

The y^2 component of e_g partial occupation forms occupied stripes pointed along local octahedra y axes, following the b lattice direction (with a small tilt) as in Fig. 4(d). The continuous stripes of y^2 character along the b lattice direction correspond to the "non-Jahn-Teller" Mn-O bonds in this direction. The Goodenough-Kanamori rules determine that the continuous stripe of y^2 character from the e_g partial occupation corresponds to AFM superexchange. The AFM coupling is along the b lattice parameter direction, between the FM coupled ac planes. Together the in-plane FM and interplane AFM produce the A-AFM ground state of $LaMnO_3$, so our $U|J = 8|2$ eV calculation results are in-line with experiment as well.

If instead the Hund's coupling was weaker (i.e., smaller J), then π^{e_g} would also be smaller. This alters the character of the occupied states in the e_g shell, so that orbital ordering mediated A-AFM superexchange is reduced relative to other effects such

as FM double-exchange. This explains why stabilization of A-AFM magnetic ordering (see Table IV) is only possible when the intraorbital exchange is large enough. The very small magnitude of the intraorbital exchange interaction is the origin of the incorrect FM ground state found in prior examinations [2,23,24] of LMO using standard DFT.

The improvements in the LMO description through applying exchange corrections reinforce hints by Sawada *et al.* [23], Solovyev *et al.* [2], and Hashimoto *et al.* [24], that the correct orbital and magnetic ordering in LMO requires an anisotropic intraorbital exchange correction to the DFT ground state. In what follows, we discuss further details of the electronic and crystal structure.

C. Electronic and crystal structure details

1. Orbital order

It was previously shown that applying Coulomb corrections, such as with $U|J = 8|2$ eV, corrected the LMO electronic, magnetic, and lattice structure. Further electronic structure details are shown for the LMO DOS in Fig. 5 at the $U|J = 8|2$ eV level of correction. In Fig. 5, the position of each band in the Mn DOS agree quantitatively with the optical conductivity measurements of Jung *et al.* [47]. Further experimental agreement comes from our $U|J = 8|2$ eV calculated local magnetic moment, which at $3.7\mu_B$ agrees with Eleman's measurement [51]. The U and J dependence of the local magnetic moments are shown in Fig. 6. The high sensitivity of the electronic structure of LMO to perturbations underlies in part its complex phase diagram. This is illustrated by comparing the $U|J = 8|2$ and $U|J = 8|3$ eV DOS in Fig. 5, and by examining the magnetic state of DOS near the edges of the valence band maximum (VBM) and conduction band minimum (CBM). For $U|J = 8|2$ eV, Hund's rules are obeyed as both VBM and CBM have the same spin state whereas Hund's rules are broken for $U|J = 8|3$ eV. We find that the crossover occurs at $J \approx 2.4$ eV. $LaMnO_3$ is fragile in terms of exchange: above $J \approx 2.4$ eV, we have the breakdown of

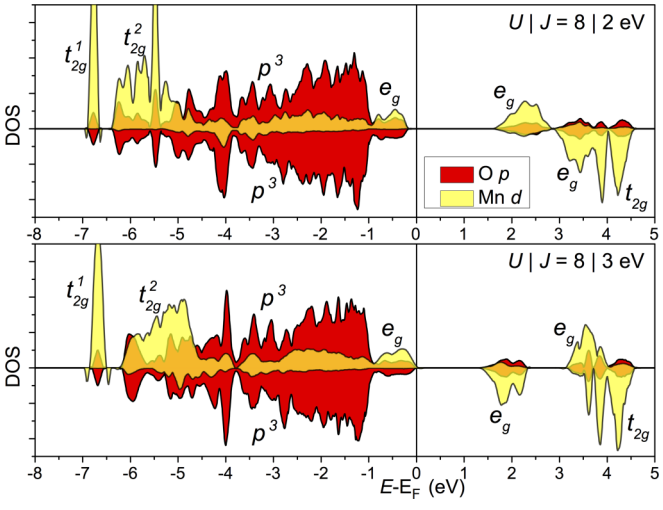

FIG. 5. (Color online) $LaMnO_3$ densities of states (DOS) for $U|J = 8|2$ and $8|3$ eV calculations. Majority spin corresponds to positive DOS and minority to negative DOS.

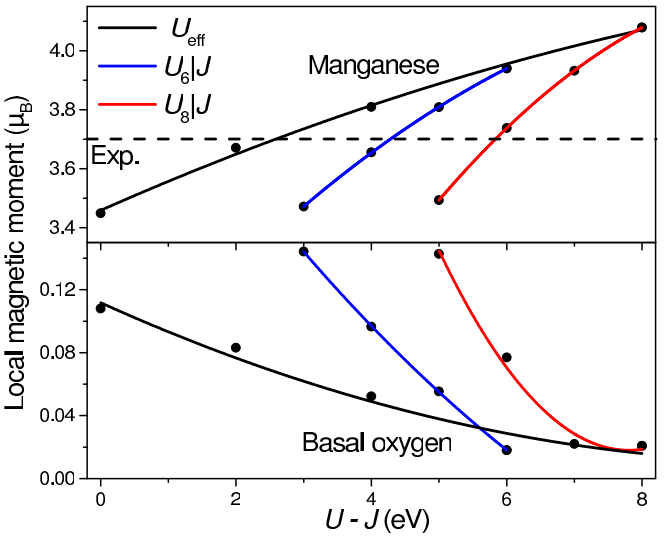

FIG. 6. (Color online) Local magnetic moment within the Bader volume for Mn cations and O anions [within the (010) basal plane], from DFT + U_{eff} and DFT + $U|J$ methods. The notation $U_6|J$ and $U_8|J$ indicates U is fixed to 6 and 8 eV, respectively, while J is varied. The experimental reference local magnetic moment is $3.7\mu_B$ [51].

Hund's rules, while below $J \approx 1.8$ eV, incorrectly stabilizes the FM rather than A-AFM ground state.

2. Magnetic coupling constants

The magnetic coupling constants in LMO have been extracted by Muñoz *et al.* [20] amongst others [2,24,49,58], by considering an Ising model (with $S = 2$ spin moment per Mn ion) for different spin-ordered solutions. The intraplane (ac) J_1 and interplane (b) J_2 coupling constants for the 20 atom LMO unit cell are

$$J_1 = \tfrac{1}{64}[E^{\text{G-AFM}} - E^{\text{A-AFM}}]$$
$$J_2 = \tfrac{1}{32}[E^{\text{A-AFM}} - E^{\text{FM}}]. \quad (11)$$

The initial A-AFM/FM stability results in Table IV hint that the coupling constants will depend strongly on the Hund's exchange parameter. In the context of previous works, J_i are well known to be highly sensitive, for example, to variation in Mn-O-Mn angle through superexchange interactions [59], and the Mn ionic charge population [58].

On the trend of magnetic stability in U and J, the superexchange interaction, which stabilizes AFM ordering, is expected to scale inversely with effective on-site Coulomb interaction, i.e., $\sim t^2/U_{\text{eff}}$ where t is effective intersite hopping. Considering first J_2 ($\sim E^{\text{A-AFM}} - E^{\text{FM}}$) in Fig. 7, the stability of AFM coupling along b decreases both with increasing U or decreasing J as expected since $U_{\text{eff}} = U - J$. However, the dependence of the J_2 coupling on U and J is not equivalent: the variation in J_2 is some fivefold more sensitive to changes in J than U, i.e., $\partial J_2/\partial J \approx -5\partial J_2/\partial U$. The AFM coupling in the ac plane, measured by J_1, is even more sensitive to the intraorbital Hund's parameter, with $\partial J_1/\partial J \approx -10\partial J_1/\partial U$. The origin of the coupling constant sensitivity to J is the strongly anisotropic effect of J on the LMO Mn d shell states,

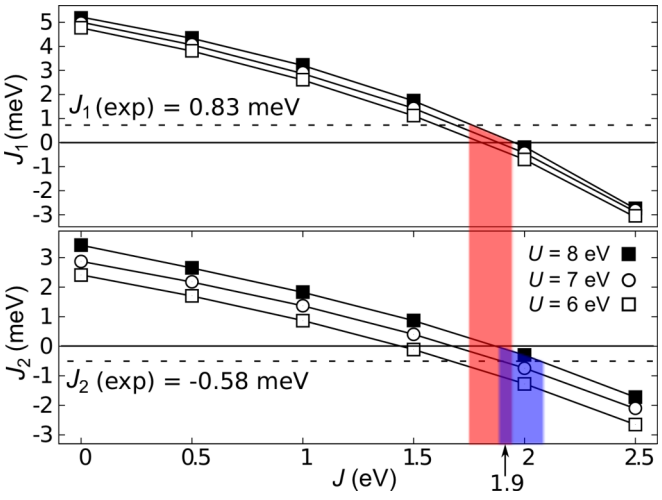

FIG. 7. (Color online) $LaMnO_3$ magnetic coupling constants J_1 and J_2 vs $U|J$ schema Hund's exchange parameter J, for $U = 6$ (white squares), 7 (white circles), and 8 eV (black squares). J_1 and J_2 are defined in Eq. (11). The red-blue overlap (centered at $J = 1.9$ eV) suggests a J exchange value for the $U|J$ scheme that provides the correct sign for both coupling constants—see main text for discussion.

with variation in J increasing π^{e_g} in Table V above and beyond that accessible with U alone.

Neutron scattering experiments have determined coupling constant values of $J_1^{\text{exp}} = 0.83$ meV and $J_2^{\text{exp}} = -0.58$ meV [60]. In Fig. 7, reasonable values for J_1 are produced with $J \approx 1.75$ eV, and for J_2 with $J_2 \approx 2$ eV. The discrepancy in J value for each J_i is perhaps unsurprising given the extreme sensitivity of A-AFM, G-AFM, and FM phases to the intraorbital Hund's interaction. Overall, the $U|J = 8|2$ eV combination previously suggested remains a good compromise at the level of half-integer eV screening intervals considered here. Although higher-resolution screening in J is beyond the scope of this work, if DFT + $U|J$ calculations are required for thermodynamic applications, the results indicate that a small modification of J by a few percent may be advantageous to tune the magnetic transition temperatures precisely, while the magnetic couplings are relatively insensitive to the direct U term.

Due to the sensitivity of the magnetic couplings to the Coulombic J correction, agreement with experiment is challenging. At $U = 8$ eV required to open the band gap, and screening in J at the half-integer intervals shown in Fig. 7, $U|J = 8|2$ eV remains the best compromise. For $U|J = 8|2$ eV, the interplane coupling at $J_2 = -0.30$ meV has the correct sign but in magnitude falls short of $J_2^{\text{exp}} = -0.58$ meV [60]. More problematic is the intraplane coupling, which overestimates the tendency for electrons to couple antiferromagnetically in the ac plane, excessively stabilizing G-AFM ordering at $J_2 = -0.19$ meV compared to $J_2^{\text{exp}} = +0.83$ meV.

In Fig. 7, the colored areas show the J values that correspond to coupling constants between zero and J_i^{exp}, i.e., the correct sign for each J_i. The overlap in colored areas identifies the narrow range of intraorbital exchange values, $1.88 \leqslant J \leqslant 1.95$ eV, that gives the correct signs for both J_i together, with $E(\text{A-AFM}) < E(\text{FM}) < E(\text{G-AFM})$ in agreement with experiment [60]. Based on the refinement in J value, we have performed GGA (PBEsol) calculations with $U|J = 8|1.9$ eV. The error in calculation results with respect to experimental values [44,47,51,60–62] is summarized in Table VI. The $U|J = 8|1.9$ eV calculations produce good experimental agreement overall, with magnetic coupling constants with signs that agree with experiment, $J_1 = +0.2$ and $J_2 = -0.1$ meV, a band gap value only a couple of percent above the experimental 1.7-eV value, and lattice parameter errors between +1.5% and −0.8%, which largely cancel to give a volume error with respect to experiment of +0.1% [47,60].

3. *Jahn-Teller distortion*

We end our analysis with conclusions on the nature of the Jahn-Teller distortion in LMO and on the origin of the LMO insulating state. The Jahn-Teller distortion in $LaMnO_3$ can be characterized in terms of two normal modes of the type introduced by van Vleck [63] and by Kanamori [64]. The normal modes are shown in Fig. 8 along with the crystal unit cell and the local octahedral basis. The modes are calculated as

$$\mathbf{Q}^{\text{Ortho}} = \frac{1}{\sqrt{2}}[\mathbf{Y}_2 - \mathbf{Y}_5 - \mathbf{X}_1 + \mathbf{X}_4],$$

$$\mathbf{Q}^{\text{Tetra}} = \frac{1}{\sqrt{6}}[2\mathbf{Z}_3 - 2\mathbf{Z}_6 - \mathbf{Y}_2 + \mathbf{Y}_5 - \mathbf{X}_1 + \mathbf{X}_4]\,.$$

Each variable represents an octahedral bond length, with subscripts indexing oxygen octahedral cage sites for a given manganese center, i ($i = 1, \ldots, 6$). In the local basis in this work, which differs from other choices [24,49,65], $\mathbf{Z}_i = \mathbf{z}_i^{\text{O}} - \mathbf{z}^{\text{Mn}}$ are the long Mn-O bonds and $\mathbf{X}_i = \mathbf{x}_i^{\text{O}} - \mathbf{x}^{\text{Mn}}$ short Mn-O bonds, with both in the FM coupled ac plane. $\mathbf{Y}_i = \mathbf{y}_i^{\text{O}} - \mathbf{y}^{\text{Mn}}$ are along the interplane AFM coupled b lattice direction.

We begin commenting that the formation of a band gap in $LaMnO_3$ is not solely electron-electron (e-e) or

TABLE VI. $LaMnO_3$ electronic, magnetic, and structural properties obtained from a $U|J = 8|1.9$ eV calculation, with comparison to experimental counterparts [44,47,51,60–62]. The $J = 1.9$ eV value is based on a refinement of the Hund's exchange parameter to secure the correct sign for both magnetic coupling constants, J_1 and J_2, which are exceptionally sensitive to on-site exchange—see Fig. 7.

	Electronic gap		Magnetic		Structural		
$U\|J$ (eV)	E^{Gap} (eV) [47]	Character [47]	J_1, J_2 (meV) [62]	M (μ_B) [51]	$\mathbf{Q}^{\text{Ortho}}$, $\mathbf{Q}^{\text{Tetra}}$ (a.u.) [44]	a, b, c (Å) [44]	V (Å^3) [44]
8|1.9	1.75	$e^1_{g\uparrow} \rightarrow e^2_{g\uparrow}$	+0.2, −0.1	3.76	0.145, 0.856	5.823, 7.642, 5.508	245
Exp.	1.7	$e^1_{g\uparrow} \rightarrow e^2_{g\uparrow}$	+0.83, −0.58	3.7	0.14, 0.78	5.736, 7.703, 5.540	245

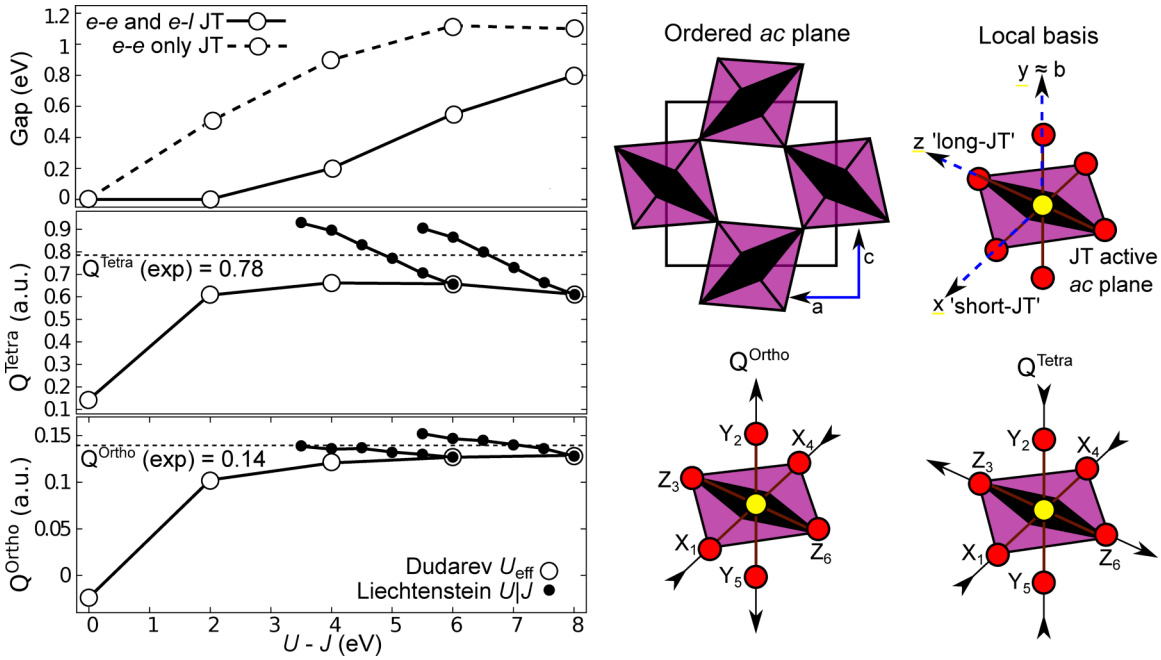

FIG. 8. (Color online) (Top left) Band gap of $LaMnO_3$ vs $U - J$ within the U_{eff} approach for fully relaxed structures where both electron-lattice and electron-electron interactions are active (dashed line, *e-l*, and *e-e*) and for structures with the Jahn-Teller distortion frozen out so only electron-electron interactions are active (solid line, *e-e* only). (Bottom left and middle) Jahn-Teller normal modes vs $U - J$ within the U_{eff} approach (white circles), and within the $U|J$ approach (black circles) for U fixed to 8 and 6 eV with J varied. (Right) Orbitally ordered and strongly Jahn-Teller active *ac* plane, the local basis convention, and $\mathbf{Q}^{\text{Ortho}}$ and $\mathbf{Q}^{\text{Tetra}}$ modes.

electron-lattice (*e-l*) in character. Rather, it is a joint function of the lattice relaxation and development of Jahn-Teller distortions as well as the strong on-site Coulomb interaction. This is illustrated explicitly in Fig. 8. As mentioned above, two logically distinct routes to breaking the symmetry exist in order to produce a gap: (i) a purely electronic effect *via* electron-electron interactions and the formation of a sizable orbital polarization π^{e_g} that breaks symmetry (also called *e-e* Jahn-Teller distortion) [55], or (ii) electron-lattice (*e-l*) Jahn-Teller distortions where certain local octahedral phonon modes become soft, the Mn-O bond lengths become unequal, and this creates crystal field symmetry breaking. These two mechanisms are in fact mutually enhancing, and which one causes which in $LaMnO_3$ is an open question that has been debated in the works of Khomskiĭ [66], Yin *et al.* [67], and Loa *et al.* [7].

In some materials, one mechanism can clearly dominate over the other. For example, in $KCuF_3$, to which $LaMnO_3$ is superficially similar as both are perovskites with partial e_g occupation, the symmetry lowering is truly driven by electronic interactions alone [22], and thus $KCuF_3$ is said to exhibit *e-e* Jahn-Teller distortion. Figure 8 shows that the nature of Jahn-Teller is different in $LaMnO_3$.

Firstly, with the *e-l* distortion frozen out, one can generate symmetry breaking and a gap for a Coulomb interaction strength ($U - J$) above a critical value $\sim$2 eV, so that, in principle, the lattice distortion is not necessary to create a gap. However, in practice, the gap and orbital splitting remain small without lattice Jahn-Teller distortions. Secondly, with $U - J$ set to zero, the DFT calculations do produce weakly active *e-l* Jahn-Teller distortions of $\mathbf{Q}^{\text{Ortho}} = -0.02$ a.u. and $\mathbf{Q}^{\text{Tetra}} = 0.14$ a.u., but the gap remains essentially zero. The addition of Coulomb repulsion *via* U_{eff} greatly enhances the *e-l* distortion of each mode to approximately $\mathbf{Q}^{\text{Ortho}} \approx 0.12$ a.u. and $\mathbf{Q}^{\text{Tetra}} \approx 0.62$ a.u.. However, even with U_{eff} applied $\mathbf{Q}^{\text{Ortho}}$ and $\mathbf{Q}^{\text{Tetra}}$ remain still short of experiment by some 13% and 20%, respectively. As per Table V and Fig. 8, one can only go so far with U_{eff}: the orbital polarization π^{e_g} is too weak and the Jahn-Teller *e-l* distortion remains largely unchanged with increasing U_{eff}.

The only way to bridge the deficit is through the use of a dedicated exchange term *via* the $U|J$ approach. As shown in Table V, J increases π^{e_g} and anisotropy throughout the d manifold significantly. By increasing J in the $U|J$ scheme, the LMO $\mathbf{Q}^{\text{Ortho}}$ and $\mathbf{Q}^{\text{Tetra}}$ modes can be tuned to agree with experiment by accessing additional *e-e* Jahn-Teller activity otherwise unavailable.

IV. CONCLUSION

An isotropic Hubbard correction, such as the U_{eff} methodology, is unable to simultaneously reproduce the band gap, the experimental level of Jahn-Teller distortion, and the magnetic ordering of bulk $LaMnO_3$. At small U_{eff}, A-AFM magnetic ordering is correctly stabilized but the gap and structural distortions are underestimated. With increasing U_{eff} values, the gap and crystal structure are reproduced but FM ordering is incorrectly stabilized. The $U|J$ approach, with its explicit exchange dependence on orbital symmetry, provides a better picture of electronic, magnetic, and structural properties of $LaMnO_3$. The origin of the $U|J$ success is the Hund's coupling accounted for by the spatial/orbital dependence of the

dedicated exchange terms that depend on J. These terms selectively polarize orbital occupation through highly anisotropic energy splitting in the Mn d manifold. Only the addition of J terms, rather than crystal field or direct Coulomb U, can provide appropriate and large enough anisotropic splitting within the t_{2g} and e_g manifolds. Orbital order due to the short-range J makes possible the combination of long-range FM exchange in the (010) plane, and AFM exchange between {010} planes, to stabilize the A-AFM ordered ground state. Soft phonon modes (*e-l* Jahn-Teller) and electronic occupation polarization (*e-e* Jahn-Teller) contribute jointly to the insulating state, with the latter being predominant. The magnitude of the experimental Jahn-Teller distortion can only be reproduced by using the anisotropic exchange correction J on top of the direct Coulomb interaction correction U. The best description of $LaMnO_3$ is achieved within the PBEsol + U framework when $U = 8$ eV and $J = 1.9$ eV.

ACKNOWLEDGMENTS

This collaborative work was funded by grants from the US's National Science Foundation (NSF-DMR MRSEC 1119826) and from the UK's Engineering and Physical Sciences Research Council EPSRC (EP/J001775/1). Via the UK's HPC Materials Chemistry Consortium, which is funded by EPSRC (EP/L000202), this work made use of HECToR and ARCHER, the UK's national high-performance computing services.

APPENDIX A: DFT + U EXPRESSIONS

We begin with the $U|J$ rotationally invariant DFT + U total energy expression [22] written for a single atomic site (since the corrections are linear sums over atomic sites),

$$E_{\mathrm{DFT}+U|J} = E_{\mathrm{DFT}} + E_U - E_{\mathrm{dc}}.$$

E_{DFT} is the total DFT energy using some flavor of exchange and correlation; the Coulombic $+U$ correction energy is

$$E_U = \frac{1}{2}\sum_{\sigma,\sigma',m^i} (m\sigma m''\sigma'|V|m'\sigma m'''\sigma') \times \left(\rho^{\sigma}_{m'm}\rho^{\sigma'}_{m'''m''} - \rho^{\sigma}_{m'''m}\rho^{\sigma}_{m'm''}\delta_{\sigma\sigma'}\right)$$

and the double-counting correction E_{dc} is

$$E_{\mathrm{dc}} = \sum_{\sigma}\frac{(U-J)}{2}N_\sigma(N_\sigma - 1) + \frac{U}{2}N_\sigma N_{\bar\sigma}\ .$$

In the above expressions, $V(\mathbf{r},\mathbf{r}') = 1/|\mathbf{r}-\mathbf{r}'|$ is the bare Coulomb interaction, σ labels spin where $\bar\sigma$ is the opposite spin to σ, m labels angular momentum states of the atomic shell under consideration (d orbitals for Mn in this paper), $\rho^{\sigma}_{mm'}$ is the single-particle density matrix, $N_\sigma = \mathrm{tr}(\rho^\sigma) = \sum_{m,m'}\rho^{\sigma}_{mm'}\delta_{mm'}$ is the number of electrons on the site of spin σ, and U and J are the direct and exchange Coulomb parameters.

The matrix elements of V are defined by $(m\sigma m''\sigma'|V|m'\sigma m'''\sigma') = \int dr \int dr'\ \phi^*_{m\sigma}(\mathbf{r})\phi_{m'\sigma}(\mathbf{r})\frac{1}{|\mathbf{r}-\mathbf{r}'|}\phi^*_{m''\sigma'}(\mathbf{r}')\phi_{m'''\sigma'}(\mathbf{r}')$. The matrix elements of V are further decomposed for an atomic shell with angular momentum l *via*

$$(m\sigma m''\sigma'|V|m'\sigma m'''\sigma') = \delta_{m-m',m'''-m''}\sum_{k=0}^{2l} c^k(lm,lm')c^k(lm''',lm'')F^k,$$

where c^k and F^k are standard atomic Slater angular integrals and radial integrals. For d shells, $U = F^0$, $J = (F^2 + F^4)/14$, and $F^4/F^2 = 0.625$ are the canonical choices [22]. Thus only two parameters are needed to specify the radial integrals: $F^0 = U$, $F^2 = (112/13)J$, and $F^4 = (70/13)J$.

To make progress with expressions for E_U and E_{dc}, which are given in terms of $\rho^{\sigma}_{mm'}$ and N_σ, we need to rewrite these expressions in terms of the occupancy eigenvalues of the density matrix, $f_{i\sigma}$. Denoting the eigenvectors of $\rho^{\sigma}_{mm'}$ as $\mathrm{V}^{\sigma}_{m,i}$ so that

$$\rho^{\sigma}_{mm'} = \sum_i \mathrm{V}^{\sigma}_{m,i}\ f_{i\sigma}\left(\mathrm{V}^{\sigma}_{m',i}\right)^*$$

we may insert this expansion into the expression for E_U. After some algebraic manipulations, using the fact that $c^0(lm,lm') = \delta_{mm'}$ for the $k = 0$ term and the unitarity of the eigenvector V^σ matrices, we find

$$E_U = \frac{U}{2}\left(N^2 - \sum_{i\sigma} f^2_{i\sigma}\right) + \frac{1}{2}\sum_{\sigma,\sigma',i,j}\mathrm{C}^{\sigma\sigma'}_{ij} f_{i\sigma}f_{j\sigma'} - \mathrm{X}^{\sigma}_{ij} f_{i\sigma}f_{j\sigma}\delta_{\sigma\sigma'},$$

where $N = \sum_\sigma N_\sigma$ is the total electron count on the site, and the Coulombic $\mathrm{C}^{\sigma\sigma'}$ and exchange X^σ correction matrices are given by

$$\mathrm{C}^{\sigma\sigma'}_{ij} = \sum_{k=2}^{2l} F^k \sum_{mm'm''m'''}\delta_{m-m',m'''-m''} \times (\mathrm{V}^\sigma)^\dagger_{im}c^k(lm,lm')\mathrm{V}^{\sigma}_{m'i}(\mathrm{V}^{\sigma'})^\dagger_{jm'''}c^k(lm''',lm'')\mathrm{V}^{\sigma'}_{m''j}$$

and

$$\mathrm{X}^{\sigma}_{ij} = \sum_{k=2}^{2l} F^k \sum_{mm'm''m'''}\delta_{m-m',m'''-m''} \times (\mathrm{V}^\sigma)^\dagger_{im}c^k(lm,lm')\mathrm{V}^{\sigma}_{m'j}\ (\mathrm{V}^{\sigma})^\dagger_{im'''}c^k(lm''',lm'')\mathrm{V}^{\sigma}_{m''j}\ .$$

The Coulomb correction $\mathrm{C}^{\sigma\sigma'}$ matrices have zero average over all entries, a fact easily shown by using some basic properties of the Slater angular integrals. The same can be done for the exchange correction matrices by separating out a constant term

$$\mathrm{X}^{\sigma}_{ij} = \Delta\mathrm{X}^{\sigma}_{ij} + J(1-\delta_{ij})\,.$$

Substituting this into the previous E_U expression and subtracting the double-counting term E_{dc} to cancel common terms then yields the total energy

$$E_{\mathrm{DFT}+U|J} = E_{\mathrm{DFT}} + \frac{U-J}{2}\sum_{i\sigma}\left(f_{i\sigma} - f^2_{i\sigma}\right) + \frac{1}{2}\sum_{\sigma,\sigma',i,j}\mathrm{C}^{\sigma\sigma'}_{ij} f_{i\sigma}f_{j\sigma'} - \Delta\mathrm{X}^{\sigma}_{ij} f_{i\sigma}f_{j\sigma}\delta_{\sigma\sigma'},$$

which is in the form of the DFT + $U_{\rm eff}$ (Dudarev) energy [21] plus a correction involving the $\mathrm{C}^{\sigma\sigma'}$ and $\Delta\mathrm{X}^{\sigma}$ matrices and the occupancies. Therefore the $U|J$ scheme can be viewed as a correction to the $U_{\rm eff}$ method, which includes additional Coulombic and exchange terms stemming from exchange integrals between different orbitals: this is because both $\mathrm{C}^{\sigma\sigma'}$ and $\Delta\mathrm{X}^{\sigma}$ are proportional to J, which leads to an orbital shape dependence of the Coulombic interactions on the site, something neglected by the $U_{\rm eff}$ scheme.

The correction to the eigenvalue follows from the occupancy derivative of the added terms to the DFT energy:

$$\frac{\partial(E_U - E_{\rm dc})}{\partial f_{i\sigma}} = (U-J)\left(\frac{1}{2} - f_{i\sigma}\right) + \sum_{j\sigma'} \mathrm{C}^{\sigma\sigma'}_{ij} f_{j\sigma'} - \Delta\mathrm{X}^{\sigma}_{ij} f_{j\sigma}\delta_{\sigma\sigma'}\,.$$

In what follows, it is more convenient to work with vectors and matrices. Thus if we collect all occupancies $f_{i\sigma}$ into a column vector f_σ, then the above eigenvalue correction can be more compactly written as

$$\nabla_{f_\sigma}(E_U - E_{\rm dc}) = (U-J)\left(\frac{1}{2} - f_\sigma\right) + J[\mathrm{A}^{\sigma} f_\sigma + \mathrm{B}^{\sigma} f_{\bar\sigma}],$$

where we have peeled off the constant J and also indicated same spin and opposite spin occupancy dependencies *via* the unitless matrices

$$\mathrm{A}^{\sigma} = (\mathrm{C}^{\sigma\sigma} - \Delta\mathrm{X}^{\sigma})/J$$

and

$$\mathrm{B}^{\sigma} = \mathrm{C}^{\sigma\bar\sigma}/J\,.$$

We now proceed to actual example cases to compute numerical values for the A^{σ} and B^{σ} matrices. The simplest assumption is to take the spherical harmonic states Y_{lm} as the eigenbasis of the density matrix ρ^{σ}. This means $\mathrm{V}^{\sigma} = \mathrm{I}$ and one can directly compute the matrices using numerical values for Slater angular integrals. The results are

$$\mathrm{A}^{\sigma} = \begin{array}{c|ccccc} & Y_{22} & Y_{21} & Y_{20} & Y_{2,-1} & Y_{2,-2} \\ \hline Y_{22} & 0 & -0.52 & -0.52 & 0.17 & 0.86 \\ Y_{21} & -0.52 & 0 & 0.52 & -0.17 & 0.17 \\ Y_{20} & -0.52 & 0.52 & 0 & 0.52 & -0.52 \\ Y_{2,-1} & 0.17 & -0.17 & 0.52 & 0 & -0.52 \\ Y_{2,-2} & 0.86 & 0.17 & -0.52 & -0.52 & 0 \end{array}$$

and

$$\mathrm{B}^{\sigma} = \begin{array}{c|ccccc} & Y_{22} & Y_{21} & Y_{20} & Y_{2,-1} & Y_{2,-2} \\ \hline Y_{22} & 0.72 & -0.40 & -0.63 & -0.40 & 0.72 \\ Y_{21} & -0.40 & 0.37 & 0.06 & 0.37 & -0.40 \\ Y_{20} & -0.63 & 0.06 & 1.14 & 0.06 & -0.63 \\ Y_{2,-1} & -0.40 & 0.37 & 0.06 & 0.37 & -0.40 \\ Y_{2,-2} & 0.72 & -0.40 & -0.63 & -0.40 & 0.72 \end{array}.$$

However, this basis is not the most relevant for solid state systems such as perovskite oxides. For high-symmetry situations, the eigenbasis of the density matrix will be given by t_{2g} (xy,yz,xz) and e_g $(3z^2-r^2, x^2-y^2)$ states. The conversion matrix is

$$\mathrm{V}^{\sigma} = \begin{pmatrix} 0 & 1/\sqrt{2} & i/\sqrt{2} & 0 & 0 \\ 0 & 0 & 0 & -i/\sqrt{2} & 1/\sqrt{2} \\ 1 & 0 & 0 & 0 & 0 \\ 0 & 0 & 0 & i/\sqrt{2} & 1/\sqrt{2} \\ 0 & 1/\sqrt{2} & -i/\sqrt{2} & 0 & 0 \end{pmatrix}$$

if we choose the order $(3z^2-r^2, x^2-y^2, xy, yz, xz)$. The transformed matrices are now in the more useful basis with entries

$$\mathrm{A}^{\sigma} = \begin{array}{c|ccccc} & 3z^2-r^2 & x^2-y^2 & xy & yz & xz \\ \hline 3z^2-r^2 & 0 & -0.517 & -0.517 & 0.517 & 0.517 \\ x^2-y^2 & -0.517 & 0 & 0.861 & -0.172 & -0.172 \\ xy & -0.517 & 0.861 & 0 & -0.172 & -0.172 \\ yz & 0.517 & -0.172 & -0.172 & 0 & -0.172 \\ xz & 0.517 & -0.172 & -0.172 & -0.172 & 0 \end{array}$$

and

$$\mathrm{B}^{\sigma} = \left(\begin{array}{c|ccccc} & 3z^2-r^2 & x^2-y^2 & xy & yz & xz \\ \hline 3z^2-r^2 & 1.143 & -0.630 & -0.630 & 0.059 & 0.059 \\ x^2-y^2 & -0.630 & 1.143 & 0.288 & -0.401 & -0.401 \\ xy & -0.630 & 0.288 & 1.143 & -0.401 & -0.401 \\ yz & 0.059 & -0.401 & -0.401 & 1.143 & -0.401 \\ xz & 0.059 & -0.401 & -0.401 & -0.401 & 1.143 \end{array}\right).$$

These matrices directly tell us how the $U|J$ scheme corrects the energy eigenvalues beyond the U_{eff} energy shift. For example, the diagonal entries of B^{σ} indicate that occupying any orbital pushes up the energy of the opposite spin orbitals by $1.14J$.

As another example, if we have an ion such as Mn^{4+} with a full spin-up and empty spin-down t_{2g} shell, so that $f_{\uparrow} = (0,0,1,1,1)$ and $f_{\downarrow} = 0$, then for the spin-up orbitals the energy correction beyond U_{eff} is $(0.52, 0.52, -0.34, -0.34, -0.34)J$, which destabilizes the same spin e_g and stabilizes the same spin t_{2g}, while for spin-down orbitals the situation is exactly reversed with energy correction $(-0.52, -0.52, 0.34, 0.34, 0.34)J$. A final example is a full t_{2g}^6 shell such as Co^{3+}, which gives zero correction to the U_{eff} scheme. The above two matrices form the basis for various analyses in the main text.

APPENDIX B: DENSITY MATRIX ROTATION TO LOCAL AXIS REPRESENTATION

In typical DFT + U approaches, the electronic structure is given in terms of density matrices for each subspace, e.g., the d shell. Unfortunately, the orthogonal global axial representation, which is most efficacious for computation, is often not the most convenient representation for analysis and understanding. This happens in calculations with nontrivial unit cells where inequivalent oxygen octahedra surround transition-metal ions. Octahedral rotations and tilts mean that the global axial system for the calculation, here labeled x',y',z', will differ from the native local axes, labeled x,y,z. Native axes for each octahedron point along the transition-metal–O bonds, and form the natural basis for understanding the electronic structure of the transition-metal d orbitals. We describe the details of a simple approach that rotates the density matrix, from the global to the local basis, *via* polynomial transformations, with $LaMnO_3$ as our example.

We choose a particular Mn ion and its nearest-neighbor O atoms, which identify an octahedral cage. Three Mn-O bonds are chosen that point in approximately orthogonal directions. The bonds are indexed $i = 1,2,3$, and we compute the difference vectors from the Mn to O positions: $\mathbf{u}_i = \mathbf{r}(O_i) - \mathbf{r}(Mn)$. These vectors are then normalized and define the local axes for the Mn. We create a 3×3 rotation matrix R connecting the global x',y',z' and local x,y,z systems,

$$\begin{pmatrix} x' \\ y' \\ z' \end{pmatrix} = \mathrm{R}\begin{pmatrix} x \\ y \\ z \end{pmatrix} = \begin{pmatrix} R_{11} & R_{12} & R_{13} \\ R_{21} & R_{22} & R_{23} \\ R_{31} & R_{32} & R_{33} \end{pmatrix}\begin{pmatrix} x \\ y \\ z \end{pmatrix},$$

defined by placing the unit vectors $\mathbf{u_i}$ in the columns of R. It is at this point that we choose the ordering of the unit vectors to reflect the physical questions at hand.Note, a traditional choice is to align z with the apical bond, but other choices are possible; for example, in our work, we have placed y along the non-Jahn-Teller "apical" Mn-O (see Fig. 4), while x and z span the Jahn-Teller active plane.

This rotation represents a linear polynomial transformation relating x',y',z' to x,y,z. The angular behavior of each d orbital is quadratic in the coordinates: $3z'^2 - r'^2$, $x'^2 - y'^2$, $x'y'$, $y'z'$, $x'z'$, so it is straightforward to plug in and algebraically transform the polynomials to the unprimed (local) coordinate system. Performing the substitutions, using the orthogonal nature of the R matrix, and collecting terms, we find

$$\begin{pmatrix} 3z^2-r^2 \\ x^2-y^2 \\ xy \\ yz \\ xz \end{pmatrix} = \mathrm{C}\begin{pmatrix} 3z'^2-r'^2 \\ x'^2-y'^2 \\ x'y' \\ y'z' \\ x'z' \end{pmatrix},$$

where the matrix C is

$$\mathrm{C} = \begin{pmatrix} \frac{1}{2}\left(3R_{33}^2-1\right) & \frac{1}{2}\left(R_{13}^2-R_{23}^2\right) & \frac{1}{2}R_{13}R_{23} & \frac{1}{2}R_{23}R_{33} & \frac{1}{2}R_{13}R_{33} \\ \frac{3}{2}\left(R_{31}^2-R_{32}^2\right) & \frac{1}{2}\left(R_{11}^2-R_{12}^2+R_{22}^2-R_{21}^2\right) & \frac{1}{2}(R_{11}R_{21}-R_{12}R_{22}) & \frac{1}{2}(R_{21}R_{31}-R_{22}R_{32}) & \frac{1}{2}(R_{11}R_{31}-R_{12}R_{32}) \\ 6R_{31}R_{32} & 2(R_{11}R_{12}-R_{21}R_{22}) & R_{11}R_{22}+R_{12}R_{21} & R_{21}R_{32}+R_{22}R_{31} & R_{11}R_{32}+R_{12}R_{31} \\ 6R_{32}R_{33} & 2(R_{12}R_{13}-R_{22}R_{23}) & R_{12}R_{23}+R_{13}R_{22} & R_{22}R_{33}+R_{23}R_{32} & R_{12}R_{33}+R_{13}R_{32} \\ 6R_{31}R_{33} & 2(R_{11}R_{13}-R_{21}R_{23}) & R_{11}R_{23}+R_{13}R_{21} & R_{21}R_{33}+R_{23}R_{31} & R_{11}R_{33}+R_{13}R_{31} \end{pmatrix}.$$

The matrix C is not unitary due to the fact that the bare polynomials $3z'^2 - r'^2, x'^2 - y'^2, x'y', y'z', x'z'$ are orthogonal but are not normalized. The normalization is done by averaging the squares of the functions $(3z'^2 - r'^2)/r'^2$, $(x'^2 - y'^2)/r'^2, x'y'/r'^2, y'z'/r'^2, x'z'/r'^2$ over the surface of the unit sphere. We place these averages, which are $4/5, 4/15, 1/15, 1/15, 1/15$, respectively, on the diagonals of a diagonal scaling matrix S and then form the scaled and unitary transformation matrix $\mathrm{D} = \mathrm{S}^{1/2}\,\mathrm{C}\,\mathrm{S}^{-1/2}$, which is our final matrix relating the d orbitals in primed and unprimed coordinates.

To give a feeling for how the method works, we take the experimental structure for $LaMnO_3$ crystal with $a = 5.736$ Å, $b = 7.703$ Å, and $c = 5.540$ Å, as in Fig. 1. In experimental structured LMO, consider the octahedron about the Mn atom at (0.00,0.00,2.77) Å, which has two basal oxygens at $O^1 = (1.12, -0.31, 1.26)$ Å and $O^2 = (1.75, 0.31, 4.03)$ Å, and an apical oxygen at $O^3 = (-0.07, 1.93, 2.37)$ Å. We form the normalized $\mathbf{u}_i$ vectors, compute R and then C and upon normalization find

$$\mathrm{D} = \begin{pmatrix} 0.06 & 0.04 & 0.01 & 0.23 & 0.31 \\ -0.03 & 0.16 & 0.88 & -0.24 & 0.64 \\ 0.58 & -0.74 & 0.97 & -0.09 & 0.27 \\ 0.78 & 0.54 & -0.71 & -0.19 & -0.33 \\ -0.05 & -0.20 & -2.76 & -0.29 & 0.99 \end{pmatrix}.$$

D can now be used to diagonalize the 5×5 density matrix in the subspace of the Mn d orbitals. For a DFT + $U|J$ calculation with $U = 8$ eV and $J = 2$ eV, fixed at the experimental structure, the Mn d eigensystem is

$$\phi_\sigma = \left(\begin{array}{c|ccccc} f_{i\sigma} & 0.42 & 0.96 & 0.97 & 0.98 & 0.99 \\ \hline 3z'^2 - r'^2 & 0.50 & 0.12 & 0.80 & -0.22 & -0.19 \\ x'^2 - y'^2 & 0.54 & 0.17 & -0.53 & -0.07 & -0.63 \\ x'y' & -0.10 & 0.80 & -0.02 & -0.56 & -0.21 \\ y'z' & 0.28 & -0.57 & 0.09 & 0.77 & -0.07 \\ x'z' & -0.60 & 0.11 & 0.25 & 0.21 & -0.72 \end{array}\right).$$

Here each eigenvector is a column vector with its eigenvalue $f_{i\sigma}$ provided above it. Before rotation, it is hard to easily read off the nature of each eigenstate by inspection. After rotation, the eigenvectors in the local basis are given by

$$\mathrm{D}\phi_\sigma = \left(\begin{array}{c|ccccc} f_{i\sigma} & 0.42 & 0.96 & 0.97 & 0.98 & 0.99 \\ \hline 3z^2 - r^2 & -0.17 & -0.05 & -0.07 & 0.13 & -0.97 \\ x^2 - y^2 & 0.99 & 0.05 & -0.07 & 0.03 & -0.17 \\ xy & 0.00 & -0.01 & 0.05 & -0.99 & -0.15 \\ yz & -0.03 & -0.99 & -0.09 & 0.00 & 0.07 \\ xz & 0.01 & +0.11 & -0.99 & -0.06 & 0.07 \end{array}\right).$$

The local basis eigenvectors are clearly much "purer" as each vector has a component whose magnitude is 0.97 or larger. And thus each configuration is easy to read off by inspection: the partially occupied state in the first column is essentially the $x^2 - y^2$ state while the last column shows that the $3z^2 - r^2$ has become filled. We have strong orbital polarization in the e_g manifold. This indicates the rotation to local octahedral coordinates successfully diagonalized the eigensystem, and that the local basis is physically relevant for understanding the electronic structure.

[1] C. Franchini, R. Kováčik, M. Marsman, S. Murthy, J. He, C. Ederer, and G. Kresse, J. Phys.: Condens. Matter **24**, 235602 (2012).

[2] I. Solovyev, N. Hamada, and K. Terakura, Phys. Rev. Lett. **76**, 4825 (1996).

[3] L. Feiner and A. Oleś, Phys. Rev. B **59**, 3295 (1999).

[4] A. Millis, Phys. Rev. B **55**, 6405 (1997).

[5] A. Millis, Nature **392**, 147 (1998).

[6] M. Baldini, V. Struzhkin, A. Goncharov, P. Postorino, and W. Mao, Phys. Rev. Lett. **106**, 066402 (2011).

[7] I. Loa, P. Adler, A. Grzechnik, K. Syassen, U. Schwarz, M. Hanfland, G. Rozenberg, P. Gorodetsky, and M. Pasternak, Phys. Rev. Lett. **87**, 125501 (2001).

[8] Y. Tokura, Science **288**, 462 (2000).

[9] M. Uehara, S. Mori, C. Chen, and S. Cheong, Nature (London) **399**, 560 (1999).

[10] Q. Chu, X. Wang, B. Li, F. Liu, and X. Liu, RSC Adv. **3**, 21311 (2013).

[11] M. Coey, Nature (London) **430**, 155 (2004).

[12] Y. Tokura, Rep. Prog. Phys. **69**, 797 (2006).

[13] H. Chen and S. Ismail-Beigi, Phys. Rev. B **86**, 024433 (2012).

[14] J. He and C. Franchini, Phys. Rev. B **86**, 235117 (2012).

[15] G. Rao, J. Sun, K. Bärner, and N. Hamad, J. Phys.: Condens. Matter **11**, 1523 (1999).

[16] N. Mathur, G. Burnell, S. Isaac, T. Jackson, B. Teo, J. MacManus-Driscoll, L. Cohen, J. Evetts, and M. Blamire, Nature (London) **246**, 170 (1997).

[17] R. Mahendiran, S. Tiwary, A. Raychaudhuri, R. Mahesh, and C. Rao, Phys. Rev. B **54**, R9604 (1996).

[18] J. Garcia-Barriocanal, J. Cezar, F. Bruno, P. Thakur, N. Brookes, C. Utfeld, A. Rivera-Calzada, S. Giblin, J. Taylor, J. Duffy, S. Dugdale, T. Nakamura, K. Kodama, C. Leon, S. Okamoto, and J. Santamaria, Nat. Commun. **1**, 82 (2010).

[19] H. Chen, Q. Qiao, M. Marshall, A. Georgescu, A. Gulec, P. Phillips, R. Klie, F. Walker, C. Ahn, and S. Ismail-Beigi, Nano Lett. **14**, 4965 (2014).

[20] D. Muñoz, N. Harrison, and F. Illas, Phys. Rev. B **69**, 085115 (2004).

[21] S. Dudarev, G. Botton, S. Savrasov, C. Humphreys, and A. Sutton, Phys. Rev. B **57**, 1505 (1998).

[22] A. Liechtenstein, V. Anisimov, and J. Zaanen, Phys. Rev. B **52**, R5467 (1995).

[23] H. Sawada, Y. Morikawa, K. Terakura, and N. Hamada, Phys. Rev. B **56**, 12154 (1997).

[24] T. Hashimoto, S. Ishibashi, and K. Terakura, Phys. Rev. B **82**, 045124 (2010).
[25] M. Wu, E. Benckiser, M. Haverkort, A. Frano, Y. Lu, U. Nwankwo, S. Bruck, P. Audehm, E. Goering, S. Macke, V. Hinkov, P. Wochner, G. Christiani, S. Heinze, G. Logvenov, H. Habermeier, and B. Keimer, Phys. Rev. B **88**, 125124 (2013).
[26] G. Kresse and J. Furthmüller, Comput. Mater. Sci. **6**, 15 (1996).
[27] G. Kresse and J. Furthmüller, Phys. Rev. B **54**, 11169 (1996).
[28] J. Perdew and A. Zunger, Phys. Rev. B **23**, 5048 (1981).
[29] J. Perdew, A. Ruzsinszky, G. Csonka, O. Vydrov, G. Scuseria, L. Constantin, X. Zhou, and K. Burke, Phys. Rev. Lett. **100**, 136406 (2008).
[30] J. Perdew, K. Burke, and M. Ernzerhof, Phys. Rev. Lett. **77**, 3865 (1996).
[31] P. Blöchl, Phys. Rev. B **50**, 17953 (1994).
[32] G. Kresse and D. Joubert, Phys. Rev. B **59**, 1758 (1999).
[33] V. Anisimov and Y. Izyumov, *Electronic Structure of Strongly Correlated Materials*, Springer Series in Solid-State Sciences Vol. 163 (Springer, Berlin, Heidelberg, 2010).
[34] V. Anisimov, F. Aryasetiawan, and A. Liechtenstein, J. Phys.: Condens. Matter **9**, 767 (1997).
[35] B. Himmetoglu, A. Floris, S. de Gironcoli, and M. Cococcioni, Int. J. Quantum Chem. **114**, 14 (2014).
[36] H. Nakamura, N. Hayashi, N. Nakai, M. Okumura, and M. Machida, Physica C: Superconductivity **469**, 908 (2009).
[37] T. Jeong and W. Pickett, J. Phys.: Condens. Matter **18**, 10529 (2006).
[38] E. Bousquet and N. Spaldin, Phys. Rev. B **82**, 220402 (2010).
[39] D. Tompsett, D. Middlemiss, and M. Islam, Phys. Rev. B **86**, 205126 (2012).
[40] B. Himmetoglu, R. Wentzcovitch, and M. Cococcioni, Phys. Rev. B **84**, 115108 (2011).
[41] T. Mellan, K. Maenetja, P. Ngoepe, S. Woodley, C. Catlow, and R. Grau-Crespo, J. Mater. Chem. A **1**, 14879 (2013).
[42] E. Cockayne and L. Li, Chem. Phys. Lett. **544**, 53 (2012).
[43] N. Kovaleva, A. Boris, C. Bernhard, A. Kulakov, A. Pimenov, A. Balbashov, G. Khaliullin, and B. Keimer, Phys. Rev. Lett. **93**, 147204 (2004).
[44] N. Sakai, H. Fjellvag, and B. Lebech, Acta Chem. Scand. **51**, 904 (1997).
[45] T. Arima, Y. Tokura, and J. Torrance, Phys. Rev. B **48**, 17006 (1993).
[46] T. Saitoh, A. Bocquet, T. Mizokawa, H. Namatame, A. Fujimori, M. Abbate, Y. Takeda, and M. Takano, Phys. Rev. B **51**, 13942 (1995).
[47] J. Jung, K. Kim, D. Eom, T. Noh, E. Choi, Y. Jaejun, Y. Kwon, and Y. Chung, Phys. Rev. B **55**, 15489 (1997).
[48] R. Krüger, B. Schulz, S. Naler, R. Rauer, D. Budelmann, J. Bäckström, K. Kim, S. Cheong, V. Perebeinos, and M. Rübhausen, Phys. Rev. Lett. **92**, 097203 (2004).
[49] J. Lee, K. Delaney, E. Bousquet, N. Spaldin, and K. Rabe, Phys. Rev. B **88**, 174426 (2013).
[50] G. Trimarchi and N. Binggeli, Phys. Rev. B **71**, 035101 (2005).
[51] J. Elemans, J. Solid State Chem. **3**, 238 (1971).
[52] Y. Nohara, A. Yamasaki, S. Kobayashi, and T. Fujiwara, Phys. Rev. B **74**, 064417 (2006).
[53] A. Georges, L. Medici, and J. Mravlje, Ann. Rev. Condens. Matter Phys. **4**, 137 (2013).
[54] F. Lu, D.-M. Chen, and L.-J. Zou, Chin. Phys. Lett. **26**, 097501 (2009).
[55] K. Kugel and D. Khomski, Sov. Phys. Usp. **25**, 231 (1982).
[56] J. Goodenough, J. Phys. Chem. Solids **6**, 287 (1958).
[57] J. Kanamori, J. Phys. Chem. Solids **10**, 87 (1959).
[58] M. Nicastro and C. Patterson, Phys. Rev. B **65**, 205111 (2002).
[59] H. Meskine, H. König, and S. Satpathy, Phys. Rev. B **64**, 094433 (2001).
[60] J. Rodríguez-Carvajal, M. Hennion, F. Moussa, A. Moudden, L. Pinsard, and A. Revcolevschi, Phys. Rev. B **57**, R3189 (1998).
[61] J. Jung, K. Kim, T. Noh, E. Choi, and J. Yu, Phys. Rev. B **57**, R11043(R) (1998).
[62] F. Moussa, M. Hennion, J. Rodriguez-Carvajal, H. Moudden, L. Pinsard, and A. Revcolevschi, Phys. Rev. B **54**, 15149 (1996).
[63] J. H. van Vleck, J. Chem. Phys. **7**, 72 (1939).
[64] J. Kanamori, J. Appl. Phys. **31**, S14 (1960).
[65] D. Khomskii, *Transition Metal Compounds* (Cambridge University Press, Cambridge, UK, 2014).
[66] D. Khomski, Phys. Scr. **72**, CC8 (2005).
[67] W. Yin, D. Volja, and W. Ku, Phys. Rev. Lett. **96**, 116405 (2006).